Fall 2021

Combined Effects of Welding Residual Stress and Thermal Expansion in CWR

Brennan Gedney

Combined Effects of Welding Residual Stress and Thermal Expansion in CWR

by

Brennan Gedney

Bachelor of Science
University of South Carolina, 2018

Submitted in Partial Fulfillment of the Requirements

For the Degree of Master of Science in

Civil Engineering

College of Engineering and Computing

University of South Carolina

2022

Accepted by:

Dimitris Rizos, Director of Thesis

Robert Mullen, Reader

Yu Qian, Reader

Tracey L. Weldon, Interim Vice Provost and Dean of the Graduate School

Dedication

In what seems to be a world constantly descending further into chaos, I find peace with those closest to me. Mom and Dad, Lee and Ryan, your unyielding love and support is far more than I will ever deserve.

Acknowledgements

Throughout the writing of this thesis, I have received a great deal of guidance and support. First and most certainly foremost, Dr. Dimitris C. Rizos. The number of times you focused my mis-directed energy is beyond count and I greatly admire your passion and approach to research. I consider myself fortunate to study under you.

I would also express the deepest gratitude to Dr. Robert Mullen and Dr. Yu Qian for applying just the right amount of stress as members of my thesis committee. Your input and expertise were incredibly helpful in this work.

To Jesús, Carolina, and Ricardo, without whom my life would be remarkably worse. Regardless of the next outcome, I thank you from the bottom of my heart.

Abstract

Continuously welded rail with flash-butt welded joints has become standard practice for railway construction around the world. Through the process of welding, a residual stress field develops in the joint which typically remains in the rail through its service life. Consequently, the total stress is altered locally in the presence of operation induced stresses. One such stress develops due to thermal expansion of the rail during the daily and seasonal solar radiation heating cycle. This paper seeks to ascertain the combined effects of welding residual stress with thermal expansion through computer simulations. This is aimed at two objectives: determining whether the combined stress fields are significant enough to be considered in rail design, and whether the deformation field is altered in a way that disrupts RNT estimations.

The first model simulates the welding process to determine the welding residual stress. The resulting stress field agrees with literature data, with notably high vertical tensile stress in the web and high compressive stress along the edges of the rail head and foot. The second model quantifies the thermal expansion occurring when rail temperature deviates from RNT. This provides a baseline of

thermal stress and thermal deformation. The presented stress field compares well with experimental data, showing negligible stress in the transverse and vertical directions while developing relatively uniform longitudinal compression. The deformation field also agrees well with the literature. The final model assesses the combination of welding residual stress and thermal expansion by incorporating the first model's resultant stress field as the initial state of the second model. With a rail temperature deviation, the total weldment stress distribution undergoes a non-uniform change despite interacting with a relatively uniform thermal stress. This simulated peak of the daily thermal stress cycle impacts the rail head, web, and foot differently. The foot experiences a fully compressive stress cycle, increasing the risk for buckling; the web undergoes a fully tensile stress cycle vertically and longitudinally that raises concerns for fatigue failures; and the head sees almost no stress cycle but retains high compression. Additionally, the profile of the top surface wave pattern is distorted when a weld is present. The high vertical tensile stress in the weldment web is identified as a key factor in this distortion.

The results show significant stress concentrations and/or stress cycles that occur in common weldment failure locations. This suggests that the combined welding residual and thermal stress fields should have greater consideration in rail design and rail fatigue life calculations. The perturbed patterns of stress and

deformation in the weldment indicates that the area adjacent to the weld should be ignored when determining the rail neutral temperature through deformation-based and stress-based methods.

Table of Contents

List of Tables

List of Figures

List of Equations

Chapter 1 - Introduction

This chapter identifies a critical problem in the rail industry and sets forth the objectives and organization of the present investigation.

1.1 Problem Statement

Railway track is manufactured in lengths of 25-120 m to allow for easy transportation to construction sites. On site, these segments are connected to form any length of track. Prior to 1900 the bolted joint connection method was used, despite high maintenance and frequent fractures. Bolted joints fell out of favor with the advent of welded joints, which offered reduced maintenance, improved dynamic behavior of the train-track-rail system, and higher allowable speeds [1]. While the first thermite welded track was built in Germany in 1899, implementation of long stretches of welded rail really began picking up steam in the 1950s.

This continuously welded rail (CWR) is now standard around the world on both transit and freight rail. While superior to jointed track, CWR is still subject to localized geometric stress, manufacturing residual stress, welding residual stress, thermal stress, bending stress, and contact stress [2]. While all of these are

significant on their own, the track becomes most vulnerable when subject to combination loading. Thermal stress from solar radiation and welding residual stresses are uniquely linked by their thermal origins and will be specifically examined in this paper.

As with any structure, connections are particularly vulnerable to common failure modes, especially as both train speeds and traffic loads are ever increasing. Indeed, each year around 15% of train derailments, which make up around 90% of total train accidents, are due to broken rails and welds [3]. The significance of the problem is slightly obscured by these statistics, seeing as many more broken rails and welds are caught on inspections and corrected before major issues arise. Both derailments and weld replacements are costly in time and money for railroad operators. This has prompted much research, which will be reviewed in Chapter 2, as detailed numerical and experimental analyses of welds are of great interest to the industry to prevent accidents and lower maintenance costs.

Axial thermal stresses pose a significant threat to the rail due to the length of rail segments. The primary concern is rail buckling from longitudinal compression. Buckled or sun-kinked rail accounts for approximately 10% of train derailments, fluctuating regionally [3]. Again, many of these rail issues are caught by inspections before accidents can occur. This is a significant issue to the industry,

as evidenced by the extensive research directed towards it, which will be discussed in Chapter 2.

Due to the cyclic, dynamic, and high magnitude nature of bending stress developed from vehicle loads, it is generally the primary load considered for rail design. The current method of rail design does not consider welding residual stress at all and only incorporates thermal stress into separate fatigue life considerations, primarily due to the relatively lower severity of these stresses. This may be an oversight because the combination of thermal stress and the initial welding residual stress might amplify or otherwise alter the total stress in and around the weldment. This combination of stresses could have a considerable influence on the bending stress used in rail design or the endurance limit used in fatigue life considerations.

A more in-depth understanding of the multi-axial stress state in the weldment is needed before a rigorous investigation can evaluate how appropriately the current method of design accounts for major sources of rail failure. These failures include buckled or broken rail, rail surface spot irregularities, and fatigue cracking, all of which are more likely to occur in the welds due to the heightened stress field and microstructural discontinuities.

1.2 Objectives of this Work

This thesis aims to clarify the combined effects of welding residual stress and thermal expansion as a first step towards a better understanding of the behavior of CWR welded joints. The objectives are:

1) Identify regions and magnitudes of stress concentrations and/or stress cycles developed by the combination of thermal loading and welding residual stress. This will be done through computer simulations.

2) Determine how thermal deformation alters stress concentrations in the weldment. This will be used to begin a discussion regarding whether these stress types should be considered more heavily in rail design.

3) Determine how the weldment stress field alters typical rail deformation. This will be used to discuss how the weld should be considered in innovative methods for RNT determination through deformation measurements.

1.3 Thesis Organization

This thesis is organized as follows: Chapter 1 identifies the problem and sets the objectives of this work. Chapter 2 presents the current state of knowledge in the field, discussing previous research that frames the importance of this investigation. Chapter 3 outlines the research approach of this work by detailing the physical system and the computer models that simulate it. Chapter 4 presents the pertinent results, the significance of which is discussed in Chapter 5. Chapter

6 states the conclusions drawn from this work and provides recommendations for future research. Appendix A contains charts that give additional detail of the welding residual stress field. Appendix B details the governing equations of the finite element code used, as a reference for future work. Appendix C explains the process by which simplified material properties were verified for use in the computer simulations.

Chapter 2 - Current State of Knowledge

Presented here is background information foundational to the current work. Overall concepts and literature review of rail welding, thermal expansion, and fatigue failure are discussed.

2.1 Rail Welding

Whenever a material is exposed to steep thermal gradients, such as in the flash-butt welding (FBW) process shown in Figure 2.1, there is opportunity for non-uniform thermal or plastic deformation on a macro scale, and phase transformation on a micro scale [4]. These cause residual stresses via local shrinkage or distortion dependent on geometry. Additionally, welding has a large number of variables (input heat variation, liquid metal behavior, solidification, material softening, exposure to ambient, etc.) that make it more difficult to determine the cause of the residual stress [4]. Over the last few decades, experimental and numerical research has been targeted towards accurate approximations of the residual stress and determining the interaction of residual stress with other sources of rail stress, which will be discussed in Section 2.1.2 and 2.1.3.

Joints in general are often regions of stress concentration, and when combined with welding induced residual stress, are often the location of brittle fracture, buckling deformation, stress-corrosion cracking, and reduced service fatigue life [5]. All this has prompted research into improving the welded joints of CWR track.

2.1.1 Flash-Butt Welding (FBW) Procedure

Among the various welding options available today, FBW is the most modern and highest-quality technique, and the advent of mobile FBW units has made this the increasingly preferred option. FBW is a resistance welding process, during which the parent rails are melted, forged together, and cooled. The entire procedure takes approximately 15 minutes in the field and can be generally separated into stages, as shown in Figure 2.1. FBW is often used in conjunction with mechanical tensioning/fastening devices to set the rail to the desired rail neutral temperature prior to fastening to the sleepers.

1) The preheating stage prepares the rail for the flashing stage and usually elevates the rail temperature to between 200 and 300 ˚C. Length of time required varies based on ambient temperature.

2) The flashing (heating) stage lasts approximately 80 seconds and is characterized by a very large average welding current and a small average upset force. Here, the parent rails are repeatedly pressed together and

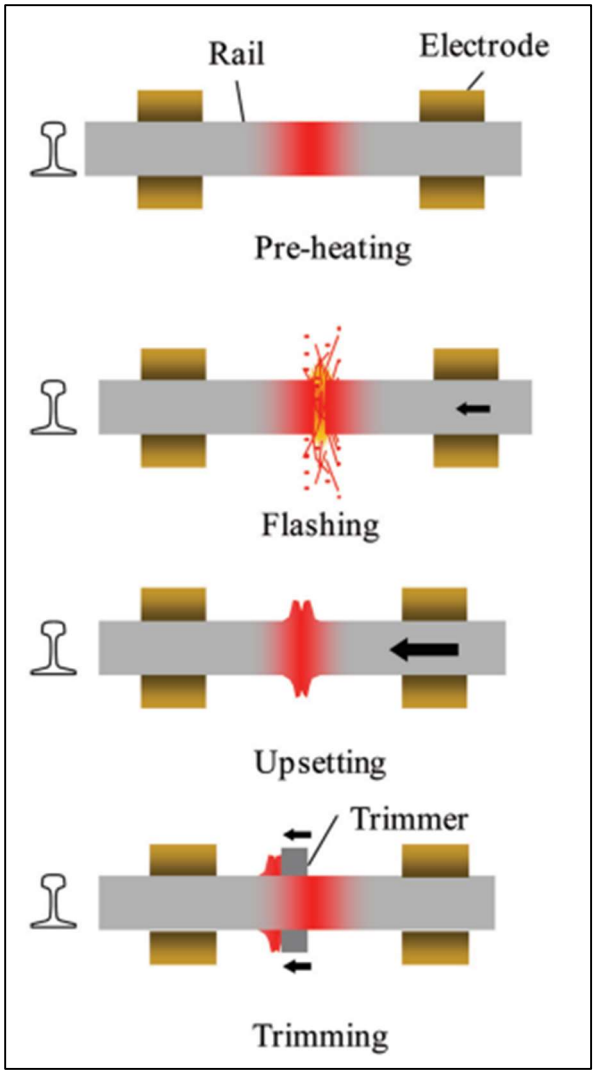

Figure 2.1: FBW process [6]

separated as the electric current passes across the interface to ensure a clean weld surface and uniform heating. By the end of this stage, a molten zone has developed at the end of each parent rail.

3) The upsetting stage lasts approximately 40 seconds and is characterized by a low average welding current, and a very high average upset force. Here, the ends of the parent rails are forged together with a large compressive force, which expels much of the molten material.

4) The cooling stage lasts approximately 980 seconds and is characterized by zero welding current, and zero upset force. Here, the residual stress field forms as the forged rails, now continuous, cool from above the melting temperature to less than 200 °C.

5) Once the cooling stage is complete, the expelled molten material that bulges from the fusion line is trimmed to establish a smooth, continuous running surface. Full cooling back to ambient temperature can take as long as 10 000 seconds, and post-weld heat treatment can delay this even longer.

2.1.2 FBW Numerical and Experimental Research

Experimental examinations of FBW welds have been the focus in recent years, as a way to verify numerical models. These include destructive techniques such as sectioning, hole-drilling, slotting, and contour, as well as non-destructive techniques such as X-ray diffraction, neutron diffraction, microscale stress, and magnetic response. The destructive techniques can only provide a few data points and are not able to capture microstresses, which can average to zero over macroscopic lengths [4]. For these reasons, focus has shifted to non-destructive methods, which have the added benefit of field applicability. Of the various non-destructive methods, diffraction techniques have taken a lead due to the ability of separating and tracking the extent and intensity of phase transformation. This

technique allows in-depth bulk analyses to be conducted on the separate components of the Cauchy stress tensor.

In 2006, Tawfik developed a procedure to utilize neutron diffraction to determine the residual stresses in large swaths of the weldment in a non-destructive way. This work was then used as a basis for papers published in 2008 and 2013 regarding the optimization of post-weld heat treatment [7][8][9][10].

From 2011 to 2015, Ma and Cai developed FEA models to build on previous work by incorporating the effects of steel phase transformation. The phase transformation was found to have quite a considerable impact on the FEA numerical results. They also proposed the use of a volumetric heat source to approximate the notoriously difficult to model electric flashing, which proved adequate. They verified their model with experimental hole-drilling results, and importantly noted the low-resolution results generated by hole-drilling. The 14 mm^2 gauges used gave a stress average and, considering the steep gradient within and near the weld fusion line, much detail is missed by the large gauges [11][12]. Because of this, numerical models should be verified by multiple experimental methods across as much of the weldment as possible, something Ma and Cai were not able to do.

In 2016, Masoudi developed a methodology for determining residual stresses from the quenching process of UIC60 rail manufacturing. The use of a heat

conduction model was well documented and very helpful as a basis for developing the methodology of the present investigation.

In 2017, Weingrill developed a FEA model of FBW with the intent of examining the temperature field variation during welding. It was determined that the complex interactions occurring within the material during phase changes have a significant influence on FEA results [13].

More recently, Oliveira analyzed an FBW joint with X-ray diffraction with the intent of developing a technique for field application. This non-destructive measurement technique was shown to be efficient and accurate [14].

2.1.3 Combination of Stresses

The highest risk to rail is combination loading due to the complex interactions of multiple stresses. The combination of residual stresses and vehicle load stresses have been specifically targeted in past research.

Skyttebol examined the growth of fatigue cracks in rail welds in 2005. This entailed numerically determining the weld residual stresses and applying axle loads to the weld. He determined that welding residual stresses had a large influence on fatigue life and that continuous weld inspection was critical because the typical crack sizes found in welds grow to failure in an exceedingly short time [1]. Since then, this paper has been the basis for many numerical analyses.

In 2014, Lee worked to optimize fatigue life assessments of welded and repair welded rail by numerically modelling the fatigue damage. By combining repair weld residual stress with wheel contact stress, a procedure to predict fatigue life was established [15].

Most recently, Sarikavak examined the influence of FBW on the microstructure and strength of rail steel. Using finite element analysis and three point bending tests, the metallurgical and mechanical aspects of welded joints were clarified [16]. Notably, the stress concentrations and microstructure of the developed finite element model were in good agreement with the experimental results.

2.1.4 Weld Improvements

The data obtained from numerical and experimental modelling is critical to research aimed at strengthening the welds in CWR.

In 2019 and 2020, Ghazanfari worked to determine the optimal flash-butt welding parameters that reduced stress in areas frequently shown to be sites of crack initiation (web and rail head). They varied maximum temperature in the rail, total welding time, upset force time and magnitude in order to minimize the size, microstructural variation, and even the hardness of the heat affected zone. The numerical models showed the welding parameters have a decisive influence on

joint quality, significantly increasing strength when these parameters were optimized [17][18]. Typical industry parameters are shown in Figure 2.2.

Mechanical and even thermal tensioning of the weld joints during or after welding are promising techniques to reduce residual stress [5]. Post-weld heat treatment is aimed at slowing the rate of cooling to around 1 ˚C h/25mm of steel thickness, roughly 1 ˚C/s [4]. Lowering the thermal gradient reduces some residual stresses by cooling the rail more evenly.

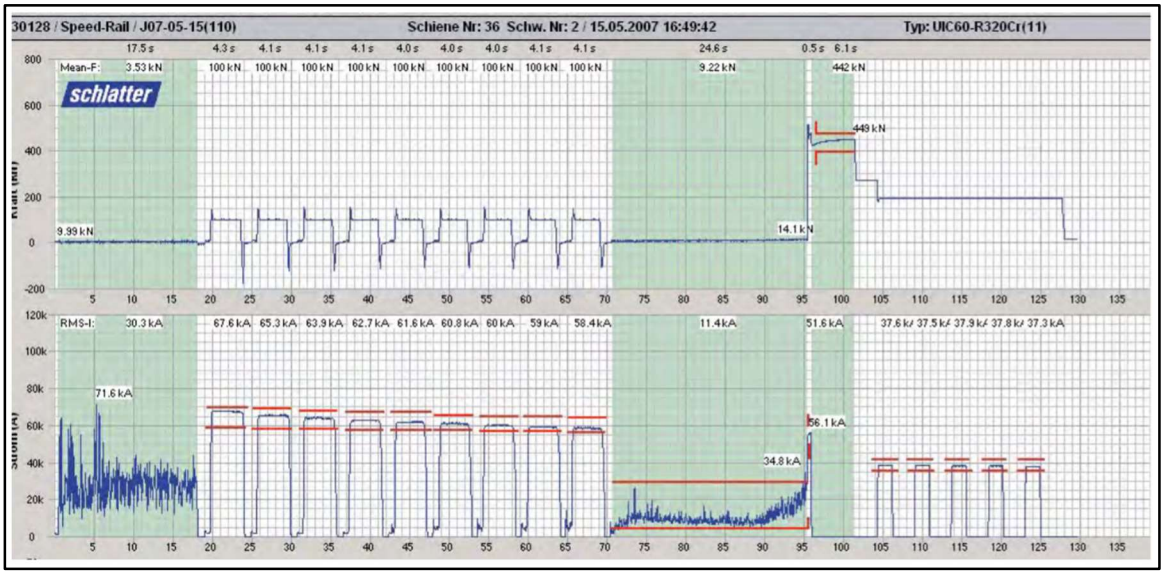

Figure 2.2: Schlatter mobile FBW machine upset force (top) and input current (bottom) [19]

There is interest in engineering a filler material composition for fusion welding. Both experimental and theoretical calculations conducted by Murakawa in 2013 have indicated that an appropriately engineered filler material can counter local tensile residual stress by using varied solid-state phase transformations to reach a local stress equilibrium [20].

While most research is targeted at strengthening the weld itself, recently some innovative external bracing concepts have been discussed. In 2020, Xiao proposed a concrete-steel brace that attempts to distribute the stresses from the axle loading to a larger portion of the rail, thus reducing the peak stress in the weldment [21].

2.2 Rail Thermal Expansion

The open-air nature of railway is important to note because of the exposure to solar radiation, seen in Figure 2.3, which results in thermal expansion.

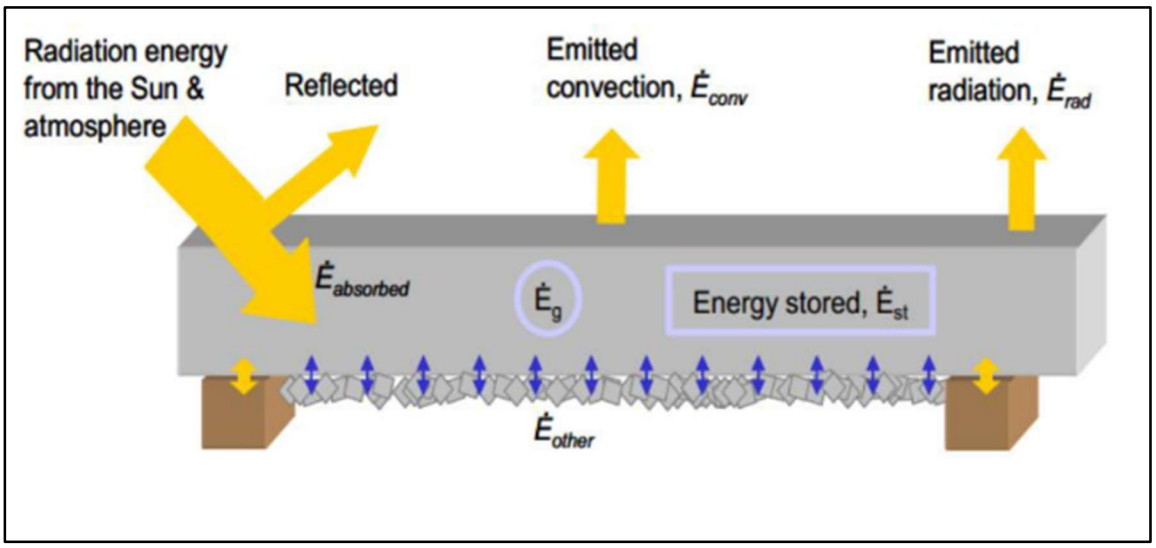

Figure 2.3: Typical rail thermal action [22]

Depending on climate, it is not uncommon to have air temperature swings from -10 ˚C in the night to +30 ˚C at midday [23]. An example graph of the daily net radiation cycle is shown in Figure 2.4.

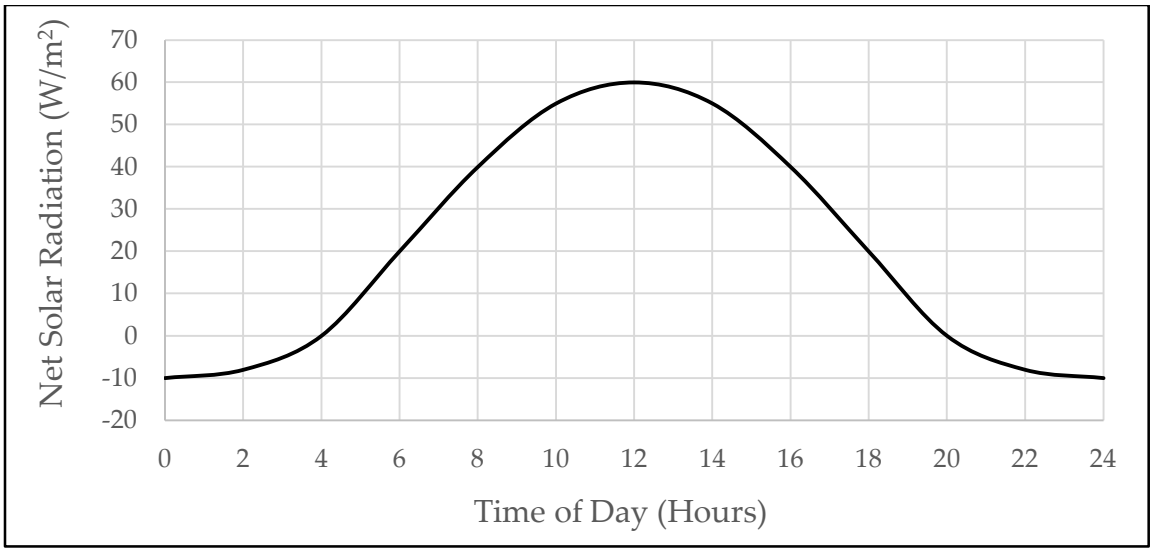

Figure 2.4: Example daily radiation cycle

The high strength steel used in rail typically has an isometric thermal expansion coefficient of around 1.2E-05 m/m/˚C, and CWR often has lengths of many kilometers. The importance of understanding and designing for rail thermal expansion can be illustrated with an example using Equation 2.1: linear thermal expansion.

$$\Delta L = \alpha L \Delta T \qquad \textit{Equation 2.1}$$

where ΔL is the change in length across the total length, L, α is the thermal expansion coefficient, and ΔT is the change in temperature.

Assuming a unit length of 1 km and an arbitrary 40 ˚C temperature swing:

$\Delta L = (1.2E-05\ m/m/^{\circ}C)(1\ km)(40^{\circ}C) = \mathbf{0.48\ m}$

This hypothetical single kilometer stretch of CWR would expand half a meter during the daily thermal cycle if completely unrestrained. However, the rail

is restrained due to operational necessity. The continuous nature of the rail constrains longitudinal movement, and the fastener/sleeper system partially constrains deformation in the transverse and vertical directions. This track configuration forces the hypothetical half meter longitudinal expansion elsewhere. In a typical rail cross-section, this manifests as high stress but low strain longitudinally and low stress but high strain transversely/vertically. Finite element analysis will be used to conduct significantly more complex calculations to ascertain the magnitude of the longitudinal stress and the transverse/vertical strain.

2.2.1 CWR Failure Modes

Of particular interest is the magnitude of the longitudinal (axial) stress, which has a large impact on the rail due to its slender nature. The two primary failure modes associated with CWR are track buckling and track pulling apart [24].

Buckling is considered the more serious of the two and occurs in high temperatures, usually in the summer, and is characterized by lateral misalignment of the rails due to deformations caused by longitudinal compression. Thermal loading can cause buckling by itself, called static buckling. However, buckling most often occurs due to combination thermal and vehicle loading, called dynamic buckling. Additionally, curves are more vulnerable to buckling due to the curvature effect, alinement imperfections, and centripetal force of vehicle loads

[25]. In 2018, Zakeri did an in-depth study and developed a definition of RNT unique to curves.

Pull apart occurs in low temperatures, usually the winter, and is characterized by fractures due to longitudinal tension [22].

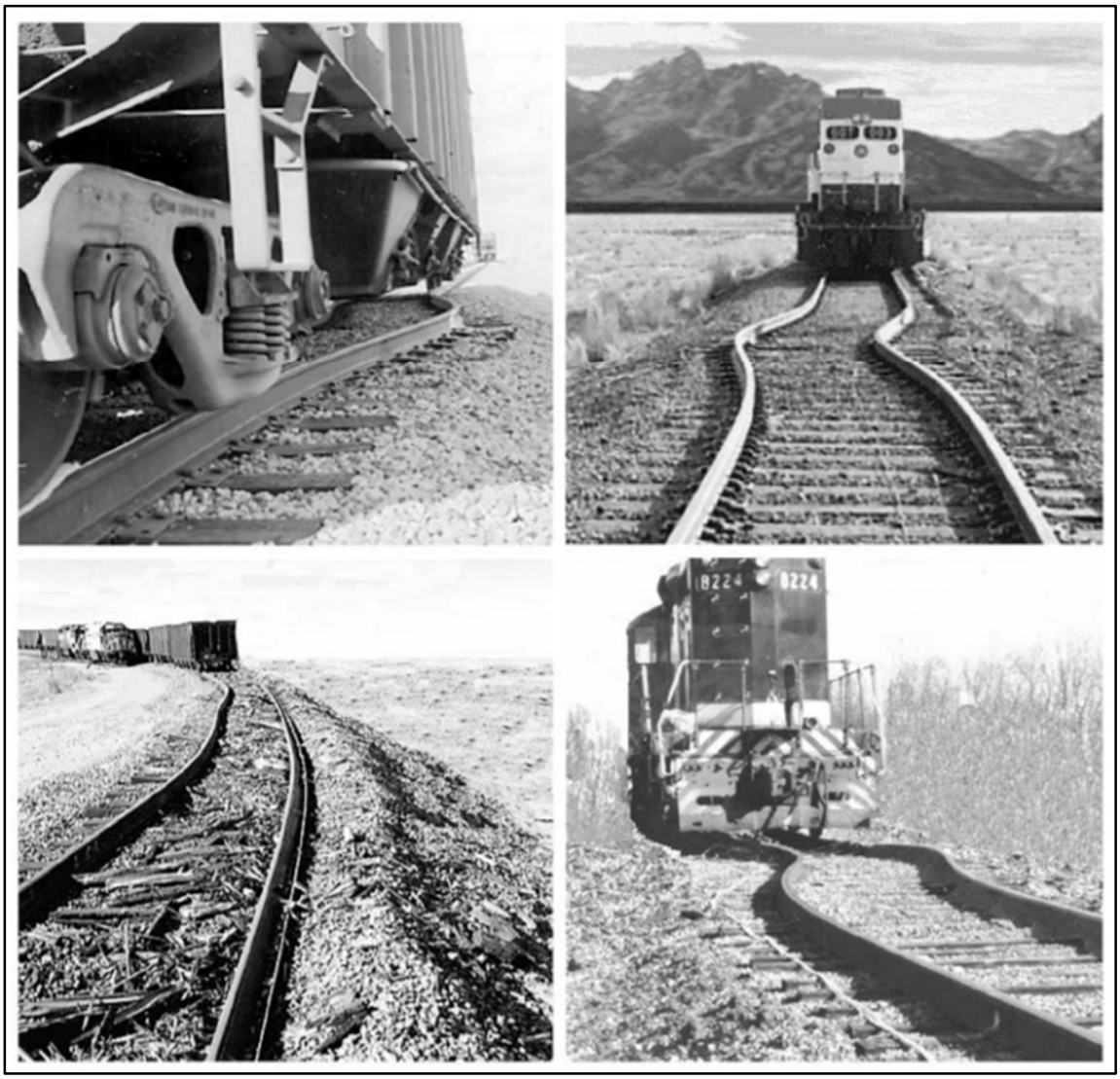

Figure 2.5: Buckled track [24]

2.2.2 *Rail Neutral Temperature*

Falling between the extremes of compression (buckling) and tension (pull apart) is a temperature at which the rail has zero longitudinal stress, called the rail neutral temperature (RNT). The theoretical RNT is dependent on climate and calculated as [6]:

$$RNT_{min} = \left(\frac{2H_t + L_t}{3}\right) + 10, \;\; RNT_{max} = \left[\left(\frac{2H_t + L_t}{3}\right) + 25\right] \pm 5 \qquad \textit{Equation 2.2}$$

where RNT_{min} and RNT_{max} are the minimum and maximum desired RNT, respectively. H_t and L_t are the highest and lowest anticipated regional rail temperatures, respectively, and are related to the minimum, $T_{air,min}$, and maximum, $T_{air,max}$, air temperature as:

$$H_t\,(^{\circ}F) \approx \frac{4}{3}T_{air,max}, \;\; L_t, (^{\circ}F) \approx T_{air,min} \qquad \textit{Equation 2.3}$$

It is important to note that the calculations for RNT do not consider any residual stresses from the manufacturing or welding process.

Ideally, rail is laid at the RNT to minimize the absolute value of temperature deviation, which corresponds to rail expansion or contraction. In practice, track is often laid at temperatures other than the RNT, which is accomplished by utilizing a longitudinal tensioning/fastening device to induce a stress correlated with the current temperature. The selected RNT is usually higher than the annual mean

temperature to account for expected reduction in the RNT caused by track maintenance, train traffic, and other factors. An RNT decrease of 17-23 ˚C (30-40 ˚F) is considered critical and requires resetting [22]. The most common form of resetting is cutting the existing rail, tensioning to desired RNT, and welding. While there are RNT reduction prevention techniques, such as low solar absorption coatings, these are difficult to implement due to the length of rail [26].

The natural RNT decrease poses a serious derailment threat to trains, and monitoring methods of a rail's in-situ, current RNT have been considered for several decades. In 1998, Szelazek utilized ultrasound to isolate the longitudinal forces by propagating shear waves in the rail height direction and longitudinal, subsurface waves along the rail. He determined that a 1 ˚C increase corresponded to approximately 2.5 MPa in longitudinal compressive stress for properly connected, tangent UIC60 rail. This type of monitoring method gained popularity due to the portability and ability to be performed without disturbing traffic [27]. Other types of techniques include cutting, lifting, deformation, ultrasonic, X-ray, vibration, and magnetic. In 2011, Arts concluded the most workable method to determine RNT is the deformation method using strain gauges, due to being non-destructive, robust for harsh track conditions, no requirement for a database, and no disruption to traffic [28]. Importantly, he noted the accuracy of deformation measurement systems was not yet proven to be high enough to be widely

implemented. This issue was addressed in 2018 by Rizos who proposed a novel deformation method of measuring RNT that has the unique characteristic of being non-contact [29]. The full-field deformations captured by thermal and 3D stereo-digital imaging are processed to quantify longitudinal stress and estimate the RNT [30]. This was verified to the viable level of accuracy that Arts concluded was required.

2.3 Rail Fatigue Failure

The average Class 1 track sees 26 million gross tons (MGT) per year, with some high tonnage track reaching 76 MGT or greater [31]. A common train is the so called "coal unit train," consisting of 100 coal cars with a gross rail load of 143 tons each (110-ton car). The typical North American car configuration transfers load to the rail through 8 wheels (2 bogies with 2 axles each). Ignoring, arguendo, the superposition of axle loads due to close spacing, the number of daily wheel passes can be calculated as:

$$Daily\ wheel\ passes = \frac{MGT * 1\ 000\ 000}{yr} * \frac{1\ yr}{365\ days} * (\#\ wheels/rail) \quad \text{Equation 2.4}$$

$$= \frac{}{(\#\ cars * car\ weight)}$$

where MGT is the annual million gross tonnage.

With 26 MGT annually, 100 cars, 143 ton cars, and 8 wheels per car:

$$Daily\ wheel\ passes = \frac{26\ 000\ 000\ ton/365}{(100 * 143\ ton)} * \left(\frac{8}{2}\right) = 1\ 992$$

Each wheel carries 1/8th the car load, or 17.9 tons in this case. This illustration shows that Class 1 rail can experience daily loading cycles in the order of magnitude of 2 000 cycles of 18 tons.

To resist these high loads, the steel used for rail is characterized by high levels of hardness (resistance to abrasion/wear/cutting), ductility (ability to deform before fracture), and toughness (resistance to fracture). Despite this high strength, fatigue is common due to the high cycle loading, typically manifesting as running surface contact fatigue and bending stress fatigue [32][33].

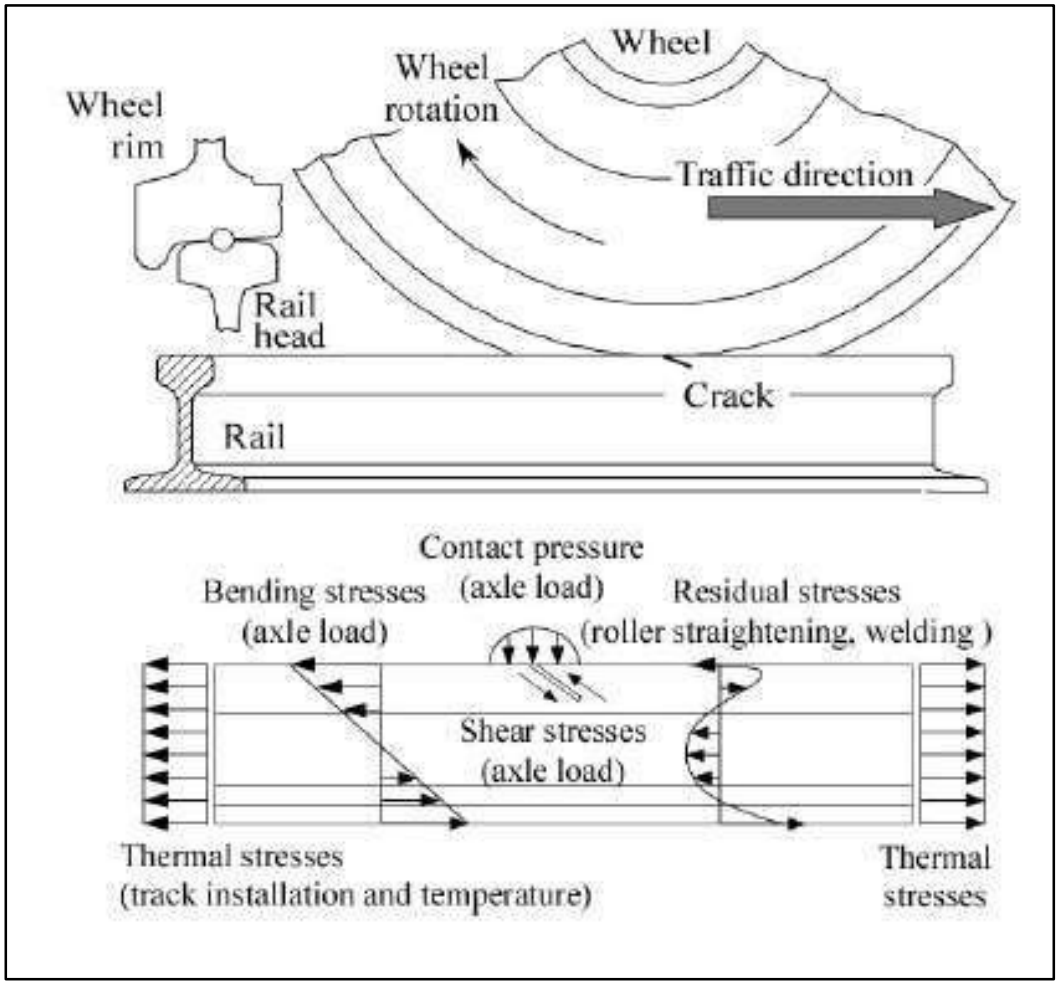

Figure 2.6: Stress diagram for typical rail [34]

2.3.1 Contact Fatigue

Contact stress at the wheel-rail interface can cause numerous types of rail wear, as well as possibly forming a plastic zone in the contact region. Rail surface spot irregularities (RSSI) are one of the most common damage conditions in rail [35]. While RSSI can occur along the entire rail, the weldments are particularly susceptible due to the presence of multi-axial stresses and microstructural discontinuities. In addition to this inherent weakness to RSSI, top surface convex irregularities commonly present on the weld even after, and perhaps because of, the post-welding rail grinding process [36]. Any irregularities on the running surface cause irregular vibrations of the wheel-rail system which, in turn, causes severe damage to the rail [37]. The geometry of the weld can be degraded over time and often grows to form saddle shapes when subject to high cycle wheel loading [36][37]. A more complete picture of the multiaxial stress state in the weld will allow more informed consideration of this problem.

2.3.2 Bending Stress Fatigue

Bending stress fatigue most commonly presents as horizontal split web or split head, as seen in Figure 2.7. This problem is difficult to correct, typically requiring replacement of the rail segment where fatigue occurs. Therefore, it is critical to initially design the rail properly to reduce the risk of having to replace the rail later on.

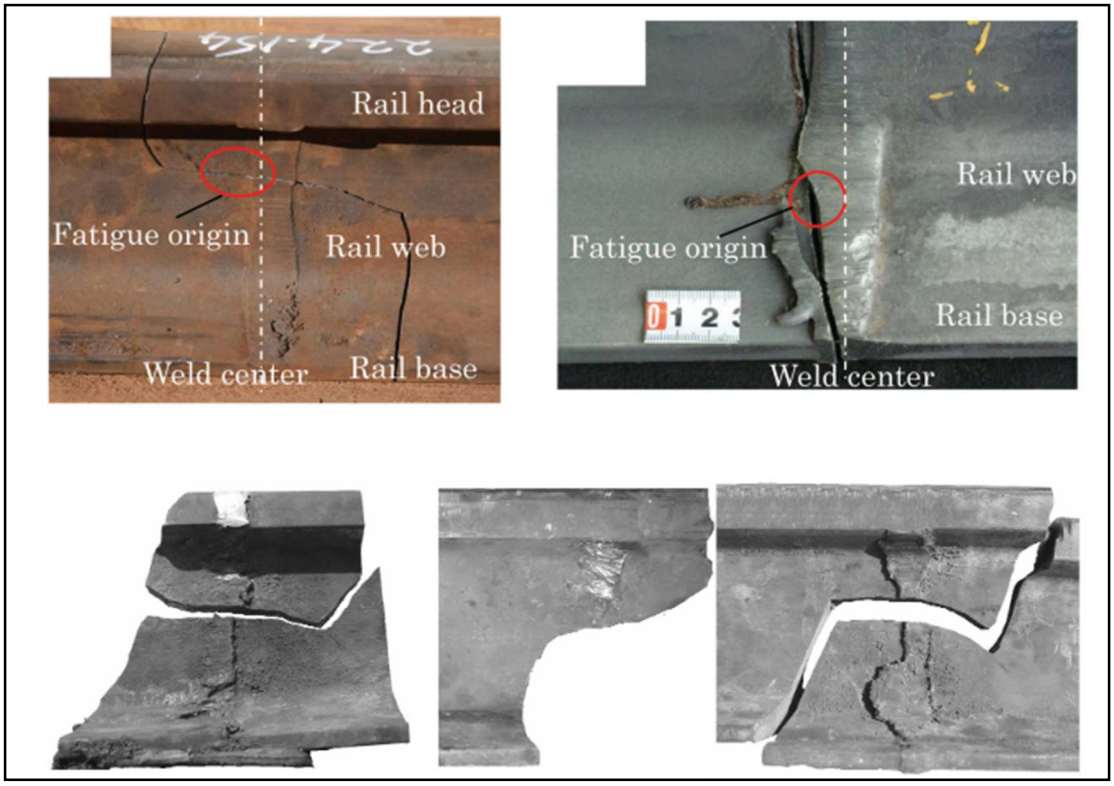

Figure 2.7: Fatigue cracking in flash-butt welds [33]

Initial design of rail includes consideration of bending stress to determine the rail shape [38]:

$$S = \frac{Pc}{I}\left(\frac{EI}{64k}\right)^{1/4} \qquad \textit{Equation 2.5}$$

where S is the rail bending stress (psi), P is the maximum wheel load (lbs), c is the distance from base to neutral axis of section (in), I is the moment of inertia of the rail section (in^4), E is the material Young's Modulus (psi), and k is the track modulus (lb/in/in).

Importantly, fatigue is not considered in this design. Instead, fatigue is a separate criterion for determining service life, with fatigue endurance limit being calculated as:

$$S_{CWR} = (\sigma_{EL} - \sigma_{R,TS})/FS \qquad \textit{Equation 2.6}$$

where S_{CWR} is the adjusted endurance limit (psi), σ_{EL} is the assumed endurance limit (psi), $\sigma_{R,TS}$ is thermal stress reduction (psi), and FS is factor of safety.

AREMA states an assumed endurance limit of 56 000 psi, a reduction of 20 000 psi for CWR, and a combined factor of safety of 1.98. This corresponds to a bending stress endurance limit of 18 000 psi (124.1 MPa) [6]. If the bending stress as calculated by Equation 2.5 is kept below this fatigue endurance limit, then rail fatigue failure is minimized.

This calculation considers thermal stresses, but not welding residual stress. Welded joints contain high residual stress fields and microstructural discontinuities that make them more susceptible to fatigue crack nucleation and growth [33]. Additionally, fatigue cracks grow exceedingly quickly [1]. This indicates there is a need to further explore how fatigue life of rail is considered in primary design.

Chapter 3 - Research Approach

This chapter details the experiments conducted for this work. This includes an explanation of the selected materials and rail configuration, which are typical to North America. Subsequently, the analysis methods and inputs of the computer simulations are detailed.

3.1 Overall Approach

The present investigation is a numerical analysis set to clarify the behavior of a weldment under the combined loading of welding residual stress and thermal stress. The intent is to provide appropriate data to include in considerations or measurements of rail neutral temperature, as well as rail design and fatigue life calculations. Three separate numerical models will be set up using the FEA program Abaqus, as delineated in Figure 3.1.

Model 1 will consist of sequentially coupled thermo-mechanical analyses simulating a flash-butt welding process conducted in the field. The key results from this model will be the welding residual stresses. Due to post-weld trimming, the deformation is assumed zero along the rail head, thus allowing deformation results from this model to be excluded from further analysis.

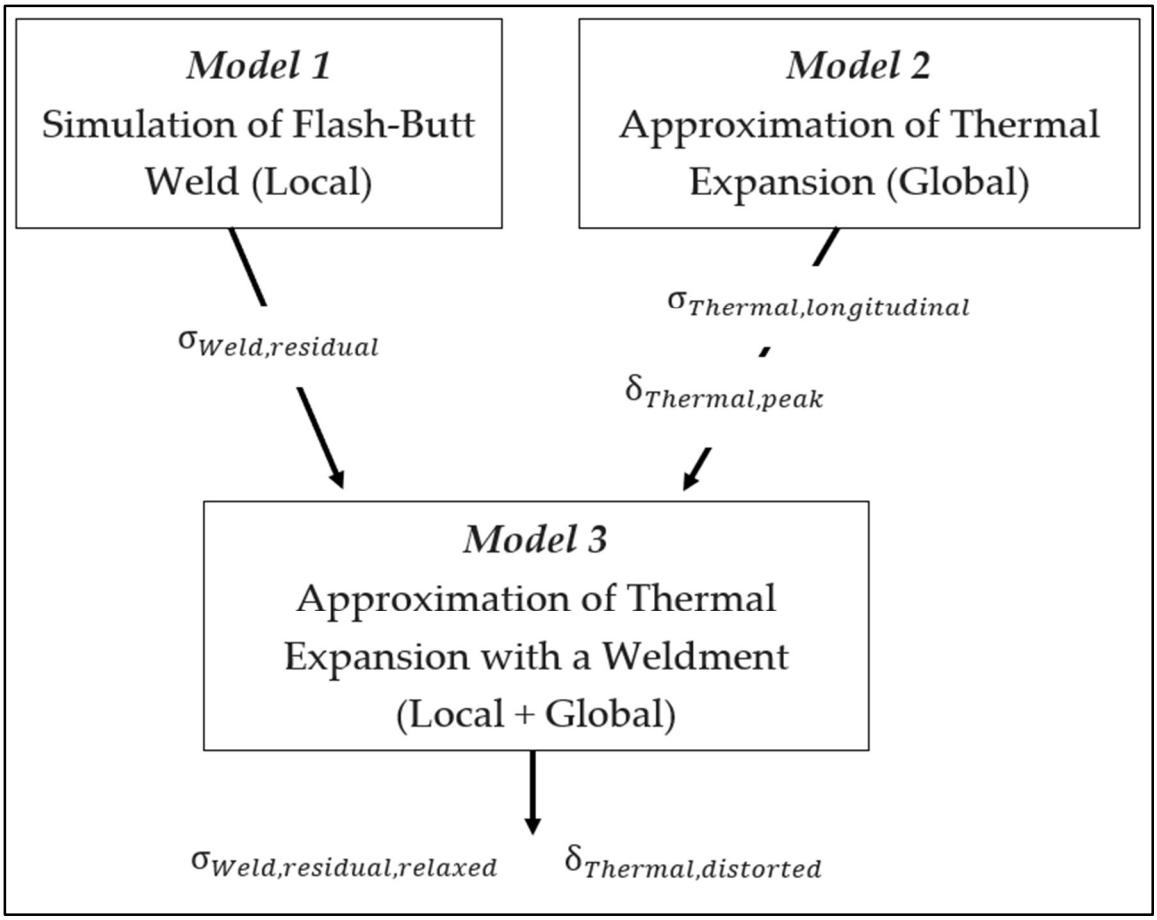

Figure 3.1: Model flowchart

Model 2 will be a fully coupled thermo-mechanical analysis of a non-welded segment of track simulating the peak thermal expansion. The main aim of this model will be to extract the thermal deformation along the top surface of the rail, as well as the thermal longitudinal stress.

Model 3 will assess the impact of welding residual stress on thermal expansion. The welding residual stress from *Model 1* will be incorporated into the layout of *Model 2*. The stresses will be extracted for comparison to the simulated welding residual stress from *Model 1*. This will be used to examine the influence of the global thermal longitudinal stress on the local welding residual stress. The

deformation along the top surface of the rail will also be extracted, for comparison to that of *Model 2*. This will be used to quantify the weldment's influence on thermal deformation.

3.2 Physical System

A typical ballasted track foundation was considered for this study. It consists of multiple layers with the main purpose of evenly distributing the axle loads from the rail to the sleepers, then to the ballast and subgrade. The complex elastic behavior of the foundation was simplified for the purposes of this study, as the main focus was the rail itself.

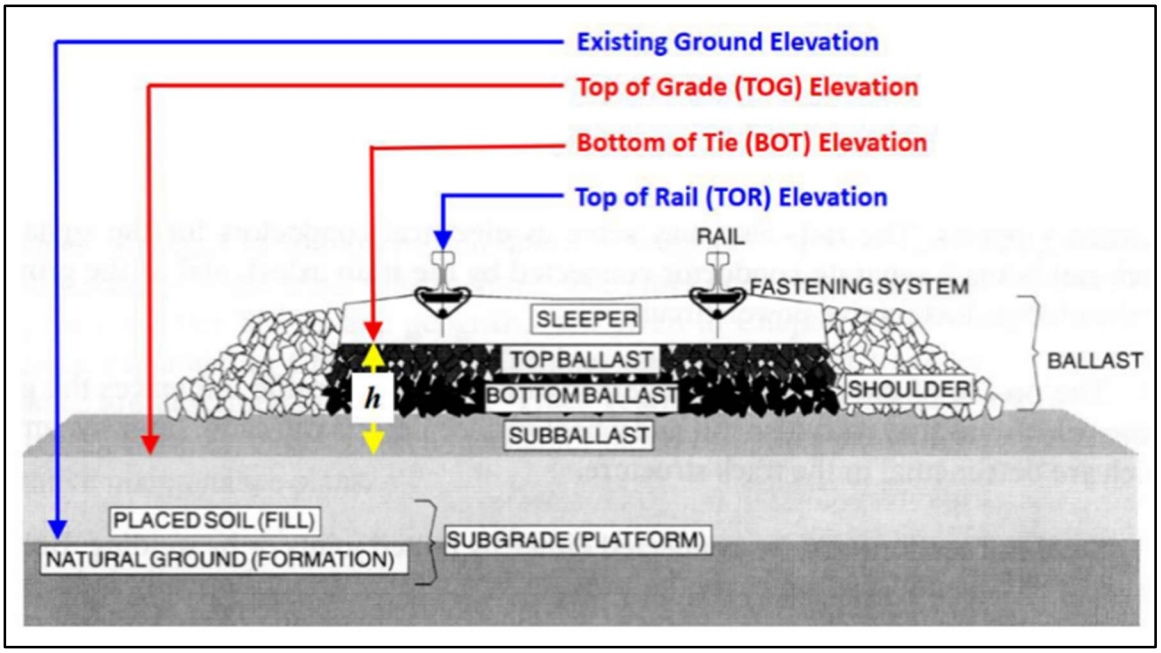

Figure 3.2: Cross-sectional view of typical rail foundation [6]

The main purpose of rail fastener systems is to ensure the rail is firmly connected to the sleepers to ensure the load properly transfers to the foundation as designed. It is also critical to maintaining gauge and restraining translational

rail movement. The complexities of the fastening system were simplified to the pertinent translational restraining nature of the system.

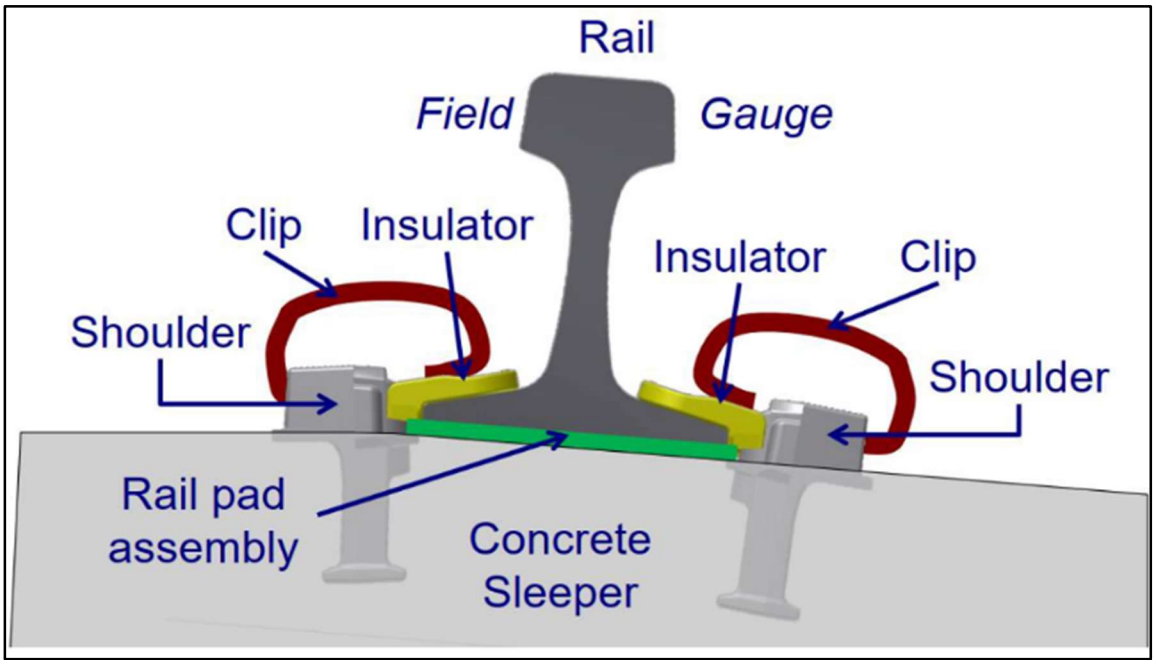

Figure 3.3: Cross-sectional view of clip style fastener system [6]

Tangent track was selected for this study to eliminate any geometric bias in the thermal expansion, as curved track has compounding effects on RNT. The rail was assumed to contain no deformities from manufacturing or welding. Concrete sleepers and Pandrol USA 'e' Clips were selected, although the properties attributed to these had little bearing on the presented analysis.

An RNT of -17 ˚C was selected as used by reference work [30]. More importantly, the maximum deviation from the RNT was selected as 60 ˚C (140 ˚F).

3.3 Analysis Methods

ABAQUS/Standard, a general-purpose finite element program, was utilized to model the physical system. The points of interest discussed below come from the Abaqus 6.11 Theory Manual [39].

Three types of models were used in the process of this investigation:

1) Heat Transfer is used to model solid body heat conduction with internal energy and general convection/radiation boundary conditions. This type of model is entirely uncoupled from mechanical analysis.

2) General Static is used to model solid body, non-inertial, static stress with general displacement/rotation boundary conditions. This model type can be sequentially coupled with a thermal time history from a Heat Transfer model.

3) Coupled Temperature-Displacement is used to model solid body stress with displacement/rotation/thermal boundary conditions, while considering the influence of the temperature field on stress/strain and vice versa. This full coupling provides more accuracy compared to a sequential coupling.

Sequential coupling (Heat Transfer → General Static) allow for faster computation time, but discounts the affects of the stress field on the temperature field or steel microstructure (Paths 2, 4, and 6 in Figure 3.4). These affects are generally small and were neglected in part of the present investigation. Full coupling does capture all of the interactions shown in Figure 3.4.

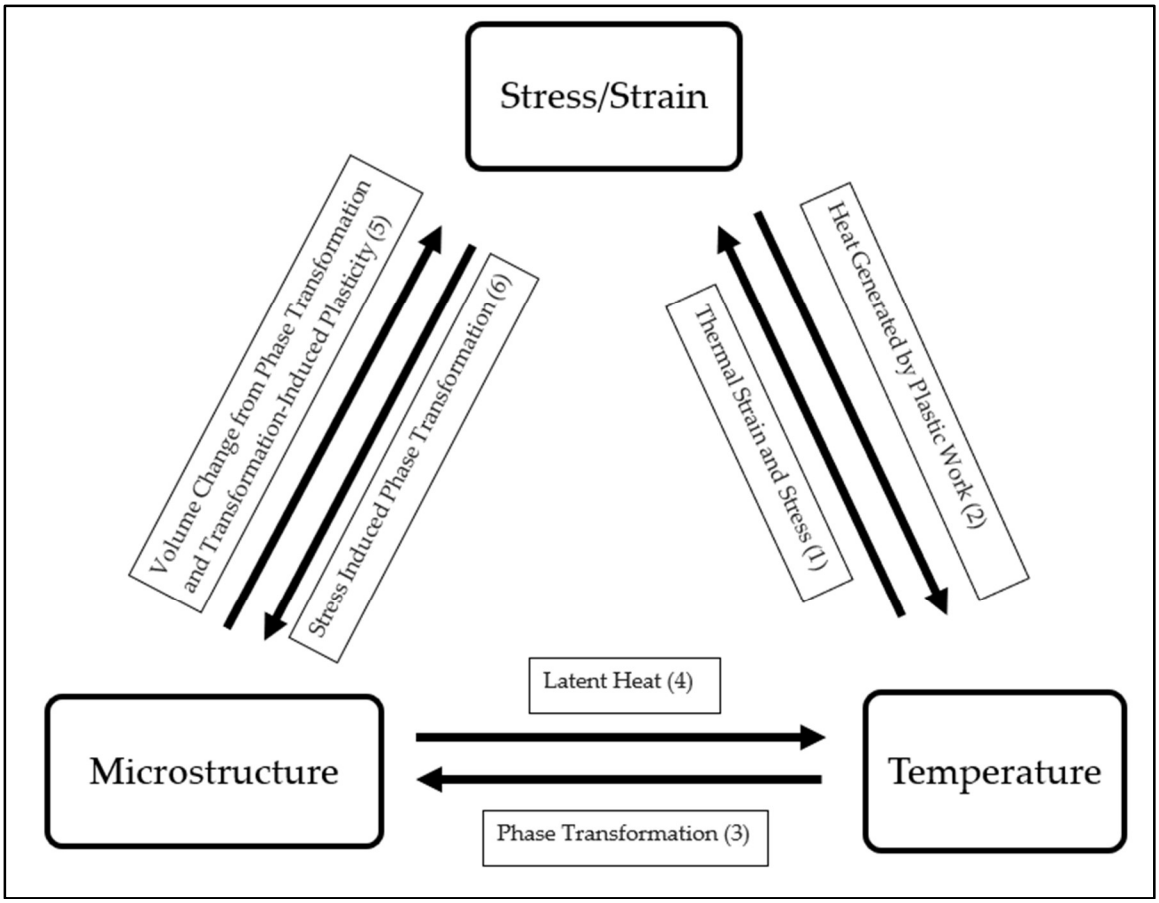

Figure 3.4: Stress/strain-temperature-microstructure interaction diagram

The governing equations of note, particularly those regarding heat, are discussed in Appendix B.

3.4 Materials

This study used 132 RE rail section, Figure 3.5, consisting of AISI 1084 steel, with properties from various sources.

Table 3.1: Chemical composition of AISI 1084 rail steel [40]

Material	Fe	C	Mn	S	P
%wt.	98.08-98.60	0.80-0.93	0.60-0.90	<0.05	<0.04

Temperature-dependent material properties provide the most accurate results for numerical analysis due to the high temperature variation of the welding

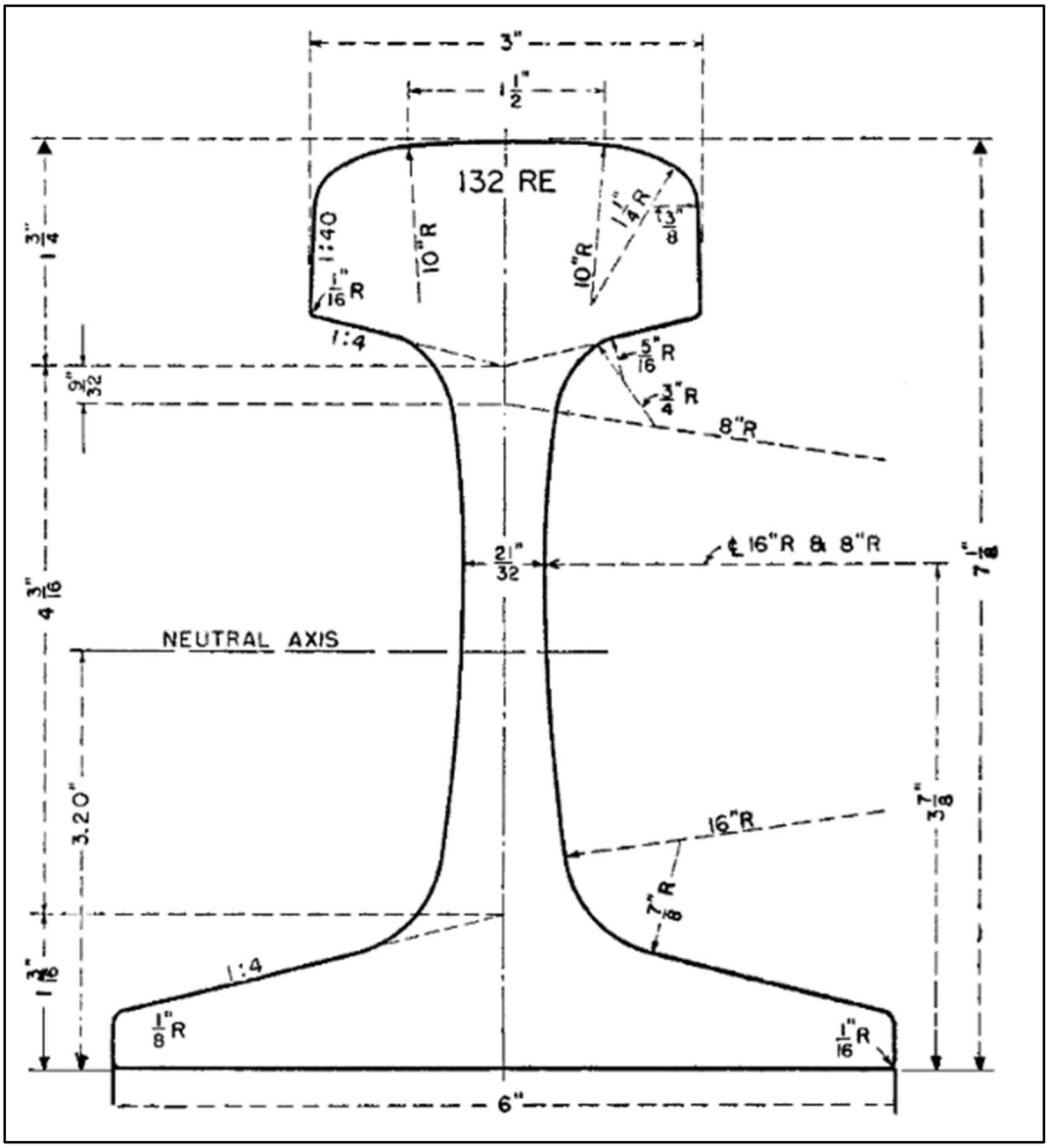

Figure 3.5: 132 RE rail [41]

process. However, high temperature material properties are difficult to obtain, and none were obtained for the steel used in this study. In 2002, Zhu investigated the effects of temperature-dependent properties on computational simulations of welding processes and determined that with the exception of yield stress, and to a lesser extent the Young's Modulus and thermal conductivity, the inclusion of temperature dependent properties on the results of simulations was negligible

[42]. They developed an engineering approach for numerical analysis of welds using simplified properties, which was verified and utilized in the present investigation (see Appendix C). All thermal and mechanical properties are taken as room temperature values, with the exception of yield and fracture stresses which are taken as simplified piecewise functions:

$$\sigma_y = \begin{cases} \sigma_{y0} = 452\ MPa \quad for \quad 0 \leq T \leq 100^{\circ}\mathrm{C} \\ \sigma_y = -0.49T + 501.4 \quad for \quad 100^{\circ}\mathrm{C} \leq T \leq 970^{\circ}\mathrm{C} \\ 5\%\sigma_{y0} = 22.6\ MPa \quad for \quad 970^{\circ}\mathrm{C} \leq T \end{cases} \qquad \textit{Equation 3.1}$$

$$\sigma_u = \begin{cases} \sigma_{u0} = 820\ MPa \quad for \quad 0 \leq T \leq 100^{\circ}\mathrm{C} \\ \sigma_u = -0.49T + 501.4 \quad for \quad 100^{\circ}\mathrm{C} \leq T \leq 970^{\circ}\mathrm{C} \\ 5\%\sigma_{u0} = 41\ MPa \quad for \quad 970^{\circ}\mathrm{C} \leq T \end{cases} \qquad \textit{Equation 3.2}$$

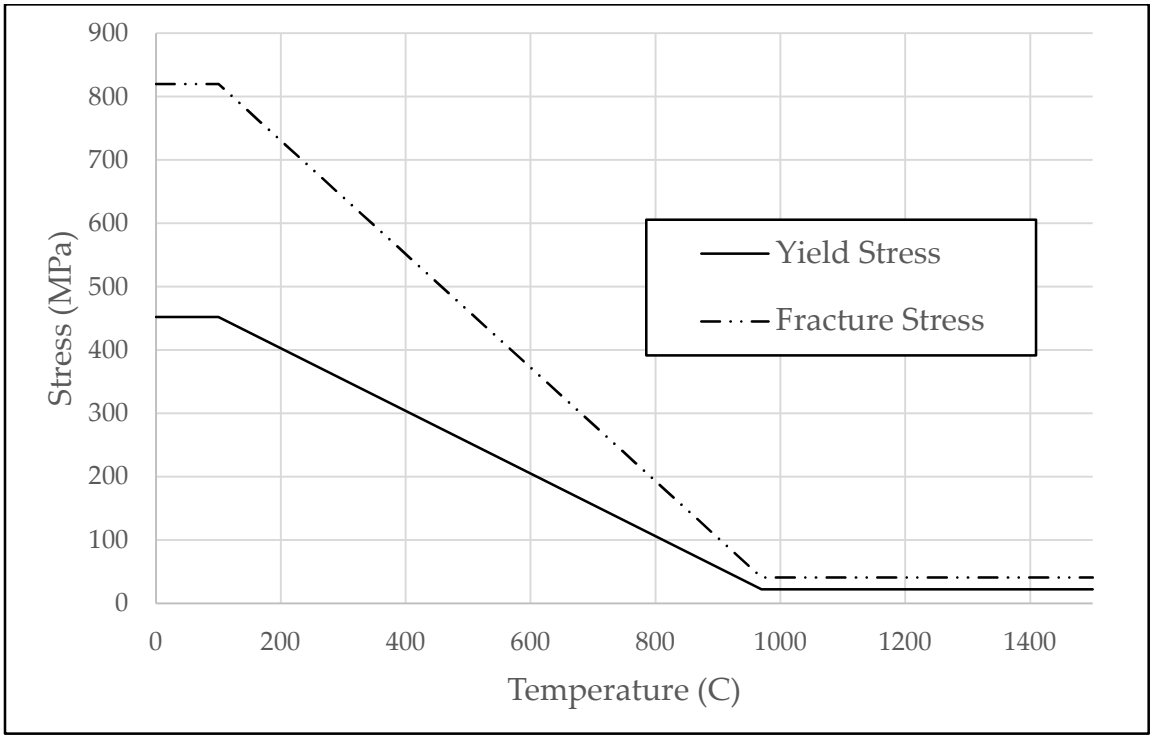

Figure 3.6: Simplified temperature-dependent yield and fracture stresses

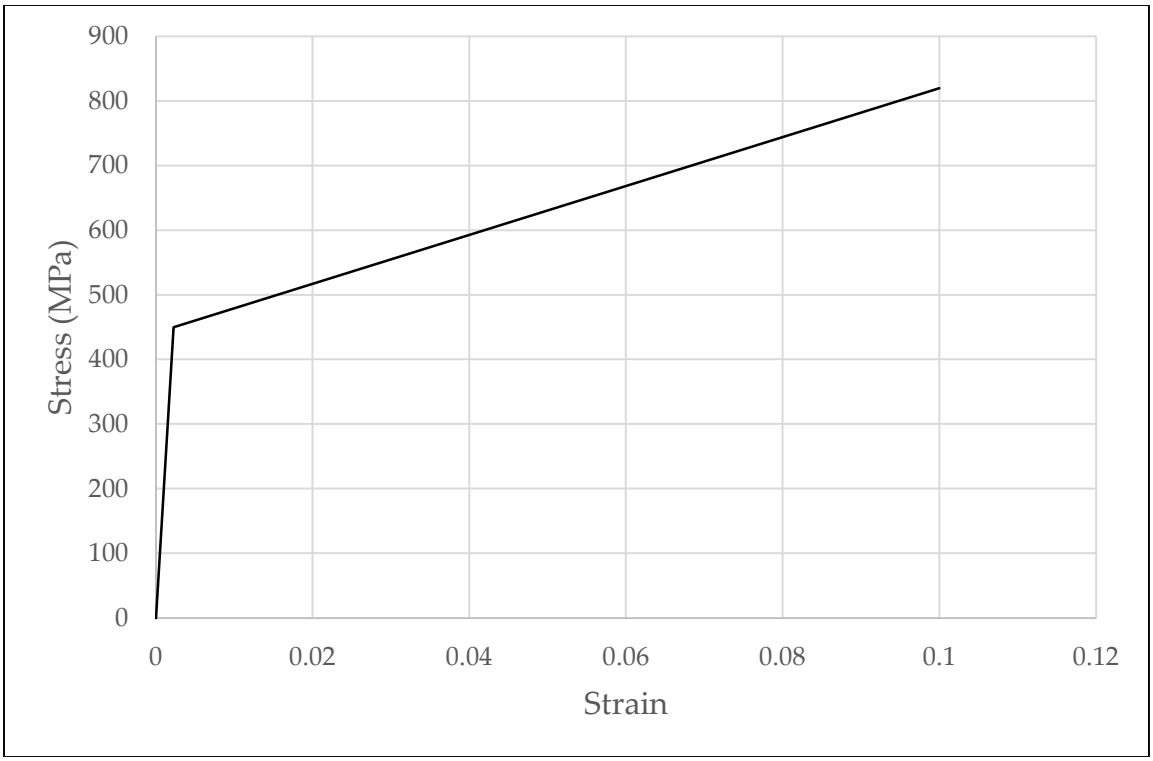

Figure 3.7: Elastic – linear strain hardening stress-strain curve at 20 °C

Table 3.2: Material properties of AISI 1084

Property at 20˚C	**Value**	**Source**
Density (kg/m^3)	7 850	[40]
Emissivity	0.96	[43]
Thermal Expansion Coefficient (m/m/˚C)	1.2E-05	[40]
Film/Convection Coefficient (W/[m^2-˚C])	27.0	[43]
Latent Heat of Fusion (J/kg)	296 000	[44]
Poisson's Ratio	0.29	[40]
Specific Heat Capacity (J/[kg-˚C])	470	[40]
Temperature of Liquidus (˚C)	1 550	[44]
Temperature of Solidus (˚C)	1 450	[44]
Thermal Conductivity (W/[m-˚C])	52	[40]
Young's Modulus (MPa)	200 000	[40]

3.5 Model 1 Layout

Model 1 consists of a sequentially coupled thermo-mechanical analysis designed to approximate the FBW procedure in the field for two, 1-m long parent rails. Considering the symmetry of the rail geometry and the thermal/mechanical loads, only one half of one parent rail was analyzed. It should be stressed that the heat source is not a part of the real-world, physical system, but rather the means to input a magnitude of heat equivalent to the real-world electric current.

Table 3.3: Model 1 mesh details

Part	Length	Elements & Type (Thermal/Mechanical)	Nodes
Rail	1.0 m	21 300 linear hexahedral (DC3D8R, C3D8R) 50 linear wedge (DC3D6, C3D6)	25 806
Molten Zone	7.0 mm	1 708 linear hexahedral (DC3D8R, N/A) 4 linear wedge (DC3D6, N/A)	2 530
Heat Source	5.0 mm	1 708 linear hexahedral (DC3D8R N/A) 4 linear wedge (DC3D6, N/A)	2 530

3.5.1 Thermal Analysis (Heat Transfer)

Table 3.4: Model 1 parameters for thermal analysis

Assembly	Heat source connected to rail (see Figure 3.8): Connected mechanically with part ties. Connected thermally with thermal interaction allowing all heat to flow.
Step	Transient response with geometric nonlinearities ignored. Direct method equation solver with default matrix storage. Full Newton solution technique. Time period: 10 000 seconds Number of increments run (automatic): 976 Initial increment size: 0.01 seconds Min. increment size: 1E-10 seconds Max. increment size: 200 seconds Max. allowable temperature change: 10 °C Max. allowable emissivity change: 0.1
Interactions	Exterior faces of the rail are subject to heat loss due to convection and radiation to ambient temperature of 20 °C.
Load	Max. volumetric heat flux of 6.05E+08 W/m^3 is applied to the heat source with the amplitude shown in Figure 3.8.
Boundary conditions	None.
Initial conditions	The rail is set with initial temperature of 300 °C to simulate preheating of the rail.
Mesh	Refined near the weld fusion line to balance computing time and accuracy. All parts are homogenous solids. See Table 3.3 and Figure 3.8.

3.5.2 Mechanical Analysis (General Static)

Table 3.5: Model 1 parameters for mechanical analysis

Assembly	Rail only. Molten zone (7 mm) removed to account for the material expelled during forging.
Step	Geometric nonlinearities accounted for. Direct method equation solver with default matrix storage. Full Newton solution technique. Time period: 10 000 seconds Number of increments run (automatic): 131 Initial increment size: 0.01 seconds Min. increment size: 1E-10 seconds Max. increment size: 200 seconds
Interactions	None.
Load	Max. upset force of 450 kN (54.01 MPa for this cross-section) applied as a compressive force on the fusion face with amplitude shown in Figure 3.8. Temperature time history of each node from the previous thermal analysis is applied as a thermal load (predefined temperature field).
Boundary conditions	XSYMM (U1=UR2=UR3=0) applied to the y-z plane interior face of the rail to reflect the symmetry across the vertical axis of symmetry. ZSYMM (U3=UR1=UR2=0) applied to the x-z plane face of the rail to reflect symmetry across the fusion line. Vertical displacement at the origin is fixed to prevent rigid body motion.
Initial conditions	None.
Mesh	See Table 3.3 and Figure 3.8.

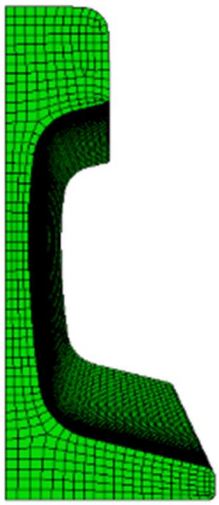

(a) Rail cross-section

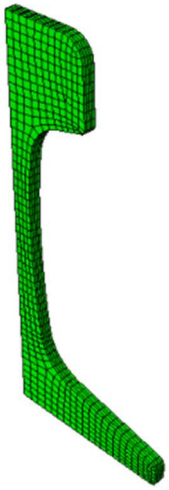

(b) Heat source

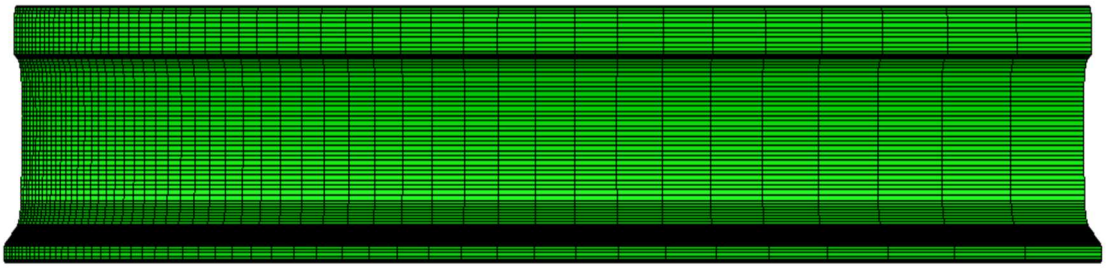

(c) Rail side view (fusion line on lefthand side)

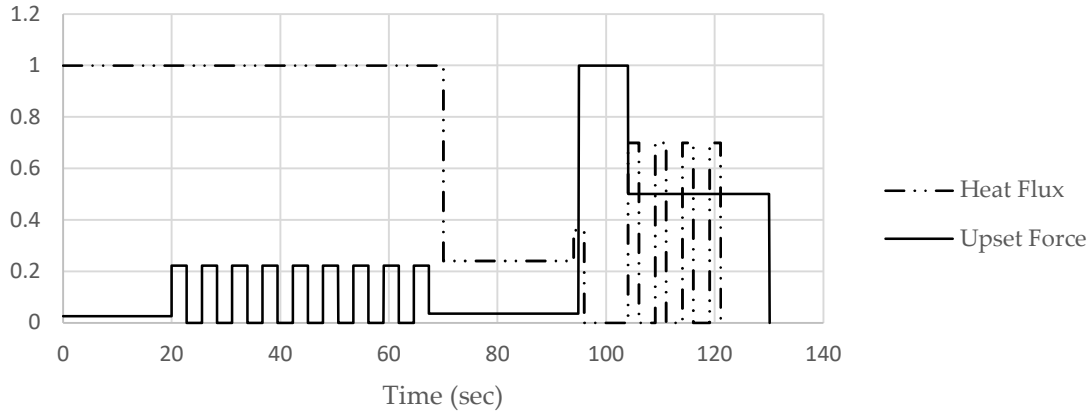

(d) Welding simulation parameter amplitudes

Figure 3.8: Model 1 layout

3.6 Model 2 Layout

A fully coupled thermo-mechanical analysis is designed to approximate the thermal expansion that occurs due to the heating of the rail during solar radiation. A surface heat flux is load stepped until the rail reaches a similar temperature as a real-world rail would be at midday, which corresponds to the height of the heating cycle and the maximum thermal expansion. This simulates a 60 ˚C deviation from the RNT.

For *Model 3*, the simulated weld will be placed at the center of this segment of rail. As the effects of the residual stress are expected to dissipate by 500 mm to either side of the weld, a 4-m long segment of rail is found to be a suitable length to analyze the problem. With this length, the rail will cross 8 sleepers, spaced 0.5 m on-center, with each sleeper fastened to the rail by a fastener clip on both the gauge and field sides.

The translational restraint aspects of the track foundation and the fastener system are simplified to frictional interactions.

The elastic effects of the track foundation are consolidated and simplified to elastic spring action in the vertical direction. The stiffness of this equivalent spring is dependent on the general track modulus and sleeper spacing as shown in Equation 3.3.

$$K_{SP} = K_{track} \cdot S_{sleeper} \qquad \textit{Equation 3.3}$$

where K_{SP} is the equivalent stiffness of the sleeper plate, K_{track} is the selected track modulus, and $S_{sleeper}$ is the sleeper spacing.

A general track modulus of 27.57 MPa (4 000 psi) is selected [30]. With a sleeper spacing of 0.5 m, the required equivalent stiffness of the sleeper plate is:

$$27.57E + 06\,\frac{N}{m^2} \cdot 0.5\,m = 13.785E + 06\,\frac{N}{m}$$

Due to procedural constraints, spring elements cannot be used simultaneously with an initial stress condition in Abaqus (which is to be used in *Model 3*). Therefore, this equivalent stiffness is attributed to the 3D solid sleeper plates using the axial stiffness equation shown in Equation 3.4.

$$K = AE/L \qquad \textit{Equation 3.4}$$

where K is the equivalent axial stiffness, A is the cross-sectional area, E is the material Young's modulus, and L is length of the object.

Using the equivalent sleeper plate stiffness as the axial stiffness, the area as the cross-sectional area of the rail seat, and the length (vertical depth) of the plate arbitrarily set at 0.01 m, calculation of the required Young's Modulus gives the desired stiffness:

$$E_{SP} = \frac{K_{SP} L_{SP}}{A_{SP}} = \frac{13.785E + 06 \frac{N}{m} \cdot 0.01\ m}{0.1492\ m \cdot 0.2159\ m} = 427\ 942.4\ MPa$$

The clipping force of the fastener system is simplified to elastic spring action normal to the rail foot top surface. A clipping force of 1.1 MPa (6 285.7 lb/in) is selected [30]. Utilizing Equation 3.4., the desired Young's Modulus is calculated:

$$E_{FC} = \frac{K_{FC} L_{FC}}{A_{FC}} = \frac{1.1E + 6\ N/m \cdot 0.01\ m}{(0.0317\ m \cdot 0.0952\ m)} = 364\ 499.1\ MPa$$

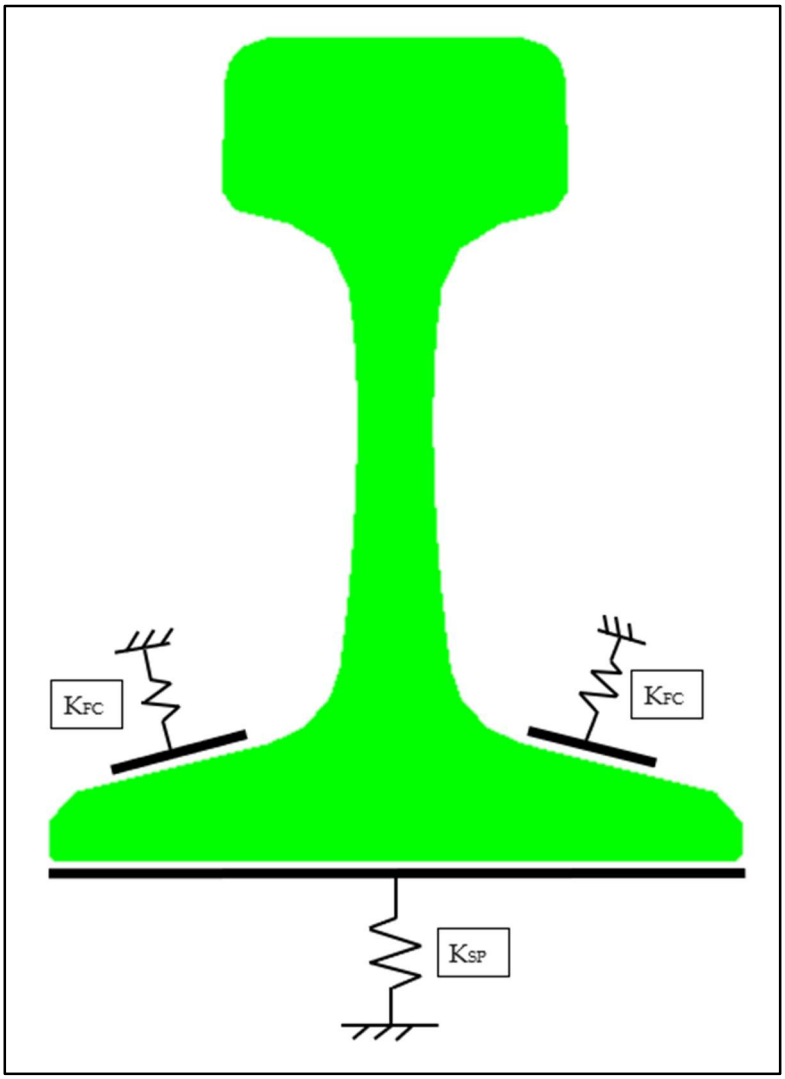

Figure 3.9: Simplified sleeper plate and fastener systems

3.6.1 Coupled Analysis (Coupled Temperature-Displacement)

The density of the rail is adjusted to 20.1 kg/m^3. Material properties of sleeper plates and fastener clips required for this type of analysis are shown in Table 3.6.

Table 3.6: Model 2 additional material properties

Property	**Sleeper Plate Value**	**Fastener Clip Value**
Density (kg/m^3)	7 850	7 850
Poisson's Ratio	0.3	0.3
Specific Heat Capacity (J/[kg-°C])	1.0	1.0
Thermal Conductivity (W/[m-°C])	1.0	1.0
Young's Modulus (MPa)	427 942.4	364 499.1

Table 3.7: Model 2 mesh details

Part	**Dimensions**	**Elements**	**Nodes**
Rail	4.0 m long	22 760 linear hexahedral (C3D8RT) 2 960 linear wedge (C3D6T)	32 728
Sleeper Plate	149.2x215.9x10 mm	2 580 linear hexahedral (C3D8RT)	4 092
Fastener Clip	31.7x95.2x10 mm	576 linear hexahedral (C3D8RT)	900

Table 3.8: Model 2 parameters

Assembly	4.0 m long rail (full cross-section). Sleeper plates spaced 0.5 m on-center, starting 0.25 m from end. Clips are centered on the top of the rail foot, at the longitudinal midpoint of the sleeper plate.
Step	Transient response with geometric nonlinearities accounted for. No automatic stabilization. The full Newton solution technique with an unsymmetric matrix solver. Time period: 1.0 (single load step) Number of increments run (automatic): 59 Initial increment size: 0.001 Min. increment size: 1E-10 Max. increment size: 1.0 Max. allowable temperature change: 10 °C
Interactions	Contact of the rail with sleeper plates and fastener clips modelled as friction with a penalty of 0.7 and normal hard contact. Small-sliding interactions implemented.
Load	Surface heat flux of 7 700 W/m^2 applied to all surfaces except the bottom of rail and rail ends.
Boundary conditions	Rail ends fixed longitudinally to simulate the continuity of the rail beyond the model. Outward faces of sleeper plates and fastener clips are fully fixed to provide reference for the "springs."
Initial conditions	Entire model set with an initial temperature of -17 °C. This is the assumed RNT as there is zero stress in the rail initially.
Mesh	The mesh is refined between the 4th and 5th sleepers to capture better detail of this region to compare to *Model 3*, which will have a weld fusion line at midspan between these sleepers. All parts are homogenous solids.

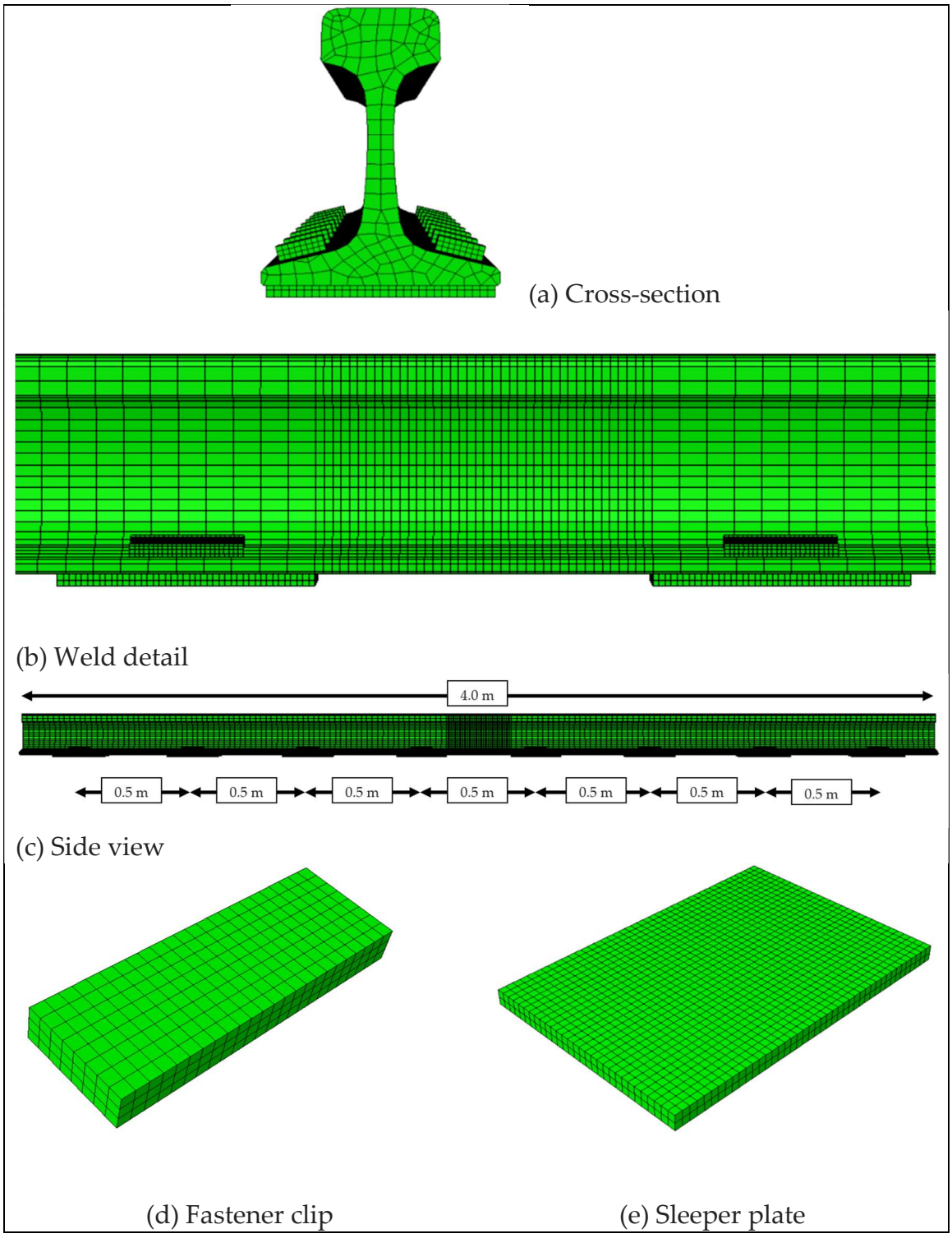

Figure 3.10: Model 2 layout

3.7 Model 3 Layout

The coupled thermo-mechanical analysis conducted in *Model 3* is identical to that from *Model 2*, with the following changes. First, the mesh of the rail between the 4th and 5th sleepers is further refined to better describe the stresses in that region. A fine mesh is required only near the fusion line to account for the steep thermal gradient and the resultant thermal strain gradient [5]. Second, the residual stresses determined in *Model 1* are imported to simulate a weld being placed midway the 4th and 5th sleepers.

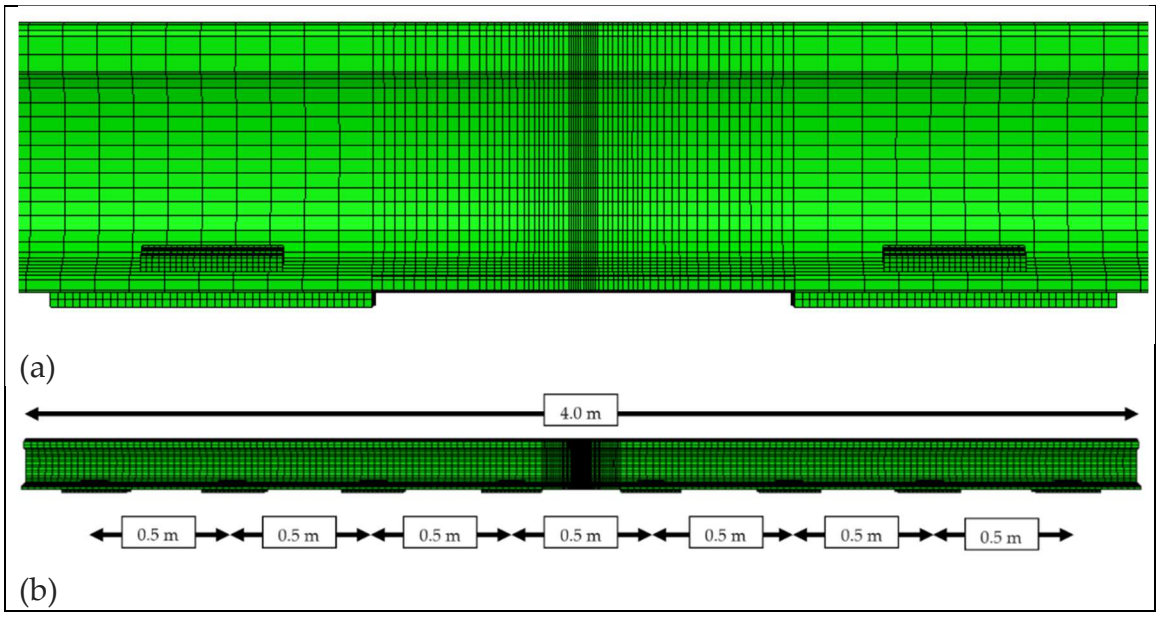

Figure 3.11: Model 3 (a) side view and (b) detail

Table 3.9: Model 3 mesh detail

Part	Dimensions	Elements	Nodes
Rail	4.0 m long	58 350 linear hexahedral (C3D8RT) 3 398 linear wedge (C3D6T)	86 961

Chapter 4 - Results

Pertinent results from the experiments detailed in Chapter 3 are presented here. The utilized conventions are explained first. This is followed by the resultant temperature, stress, and deformation fields.

4.1 Presented Results Conventions

The coordinate system and notation shown in Figure 4.1 will be used.

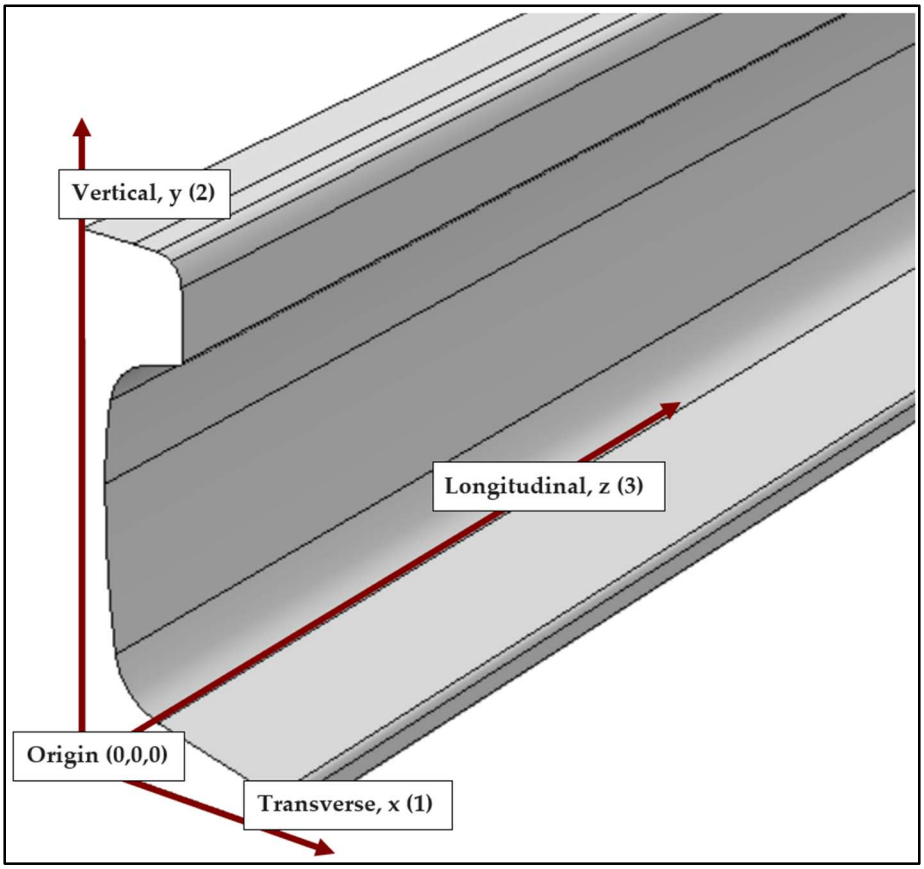

Figure 4.1: Coordinate system for presented results

Tensile stresses will be positive and compressive stresses will be negative. Stresses (σ) are presented as the components of the Cauchy stress matrix that lie along the coordinate axes, in megapascals (MPa). S11 corresponds to the stress component along the x axis, transverse on the cross-section. S22 corresponds to the stress component along the y axis, vertical on the cross-section. S33 corresponds to the stress component along the z axis, longitudinal down the rail. Deformations (δ) are presented along the coordinate axes, measured in either meters or micrometers (μm). Temperature fields are reported in degrees Celsius ($^{\circ}$C).

All visualizations are cross-sectional cuts in the x-y plane. Stress and deformation visualizations are first taken directly from the weld fusion line. For *Model 1*, this is the exposed face that represents the weld fusion line face. For *Model 2*, there is no weld, but all results are extracted from a cut directly midspan of the 4^{th} and 5^{th} sleepers. This is to compare to the results from the same cross-sectional cut in *Model 3*, which does contain a weld. Cuts are also taken 0.25 m from the weld fusion line to show the stress and deformation in the rail sitting atop a sleeper adjacent to the weld.

Residual stresses formed through the welding process will be referred to as welding residual stress, welding residual, or WR. Stress/deformation caused by thermal expansion from solar radiation will be referred to as thermal stress/deformation, thermal, or TH. The stress/deformation induced from a

combination of welding residual and thermal will be called combined stress/deformation, combined, or CB.

For the purposes of this study, the rail head, web, and foot regions are defined by height above the bottom surface of the rail, as shown in Figure 4.2b. Figure 4.2a depicts the vertical centerline of the weld fusion line (Figure 4.2c), which will be used to quantify stress and deformation magnitudes.

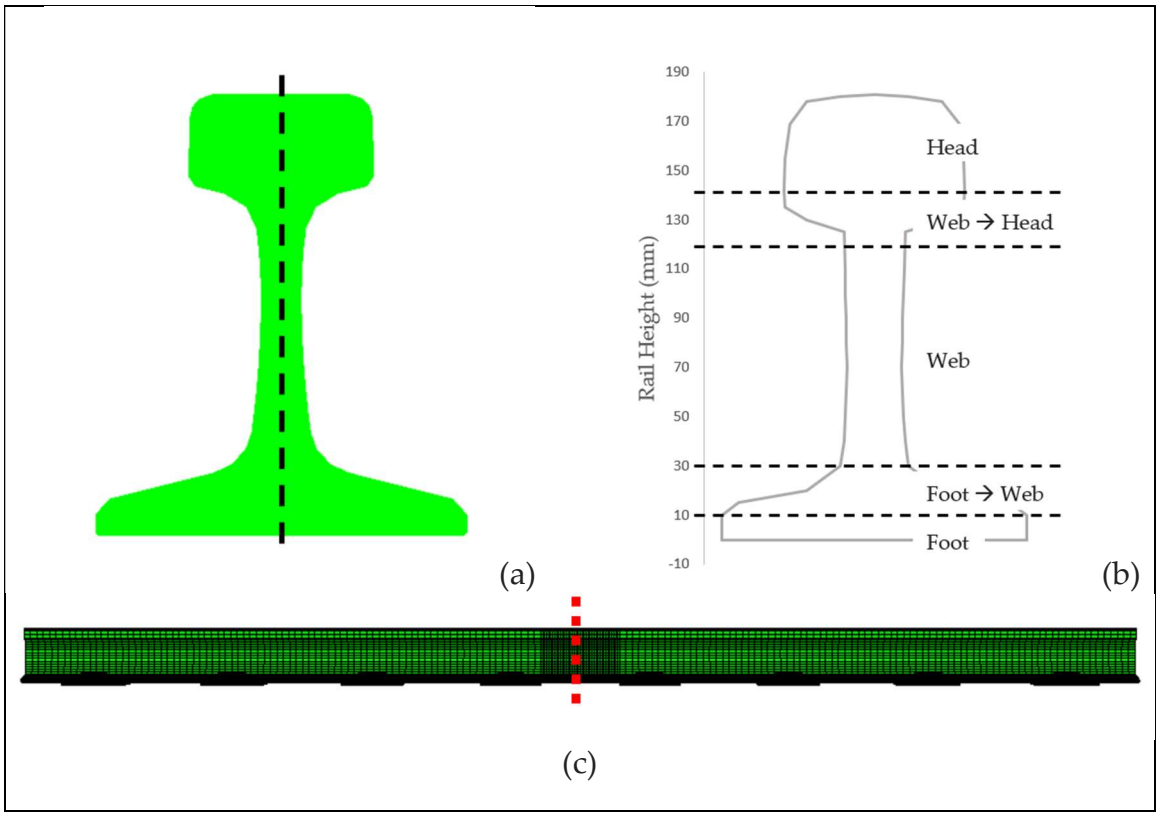

Figure 4.2: Convention definitions of rail head, web, foot, and transition regions between

4.2 Welding Temperature Field Evolution

The initial temperature for the entire rail is a uniform 300 ˚C. During welding the peak temperature reaches 1 906 ˚C, which is well above the 1 550 ˚C

temperature of liquidus for this particular steel. This produces a molten zone approximately 7 mm deep.

The thermal gradient due to uneven cooling of the rail geometry can be noted in Figure 4.3. The rail foot and web are the more exposed regions of the section and cool more quickly than the rail head. The greater ratio of steel thickness to exposed surface area in the rail head correlates to less heat loss and higher retained temperature.

The heating effects of the welding are exceedingly localized. The rail temperature beyond 150 mm from the fusion line only decreases from the initial temperature.

4.3 Peak Rail Temperature During Solar Radiation Cycle

The initial temperature for the solar radiation model is a uniform -17 ˚C. After the surface heat flux is fully load stepped, as seen in Figure 4.4, the rail head core reaches 39 ˚C, the web reaches 43 ˚C, and the rail foot core reaches 28 ˚C. The temperature variation is mostly due to different ratios of thickness to exposed surface. The surface heat flux is not applied to the bottom surface of the rail, causing the rail foot to remain cooler than the rest of the rail. The rail temperature field shown in Figure 4.4 is consistent throughout the length of the rail model at the end of the load step.

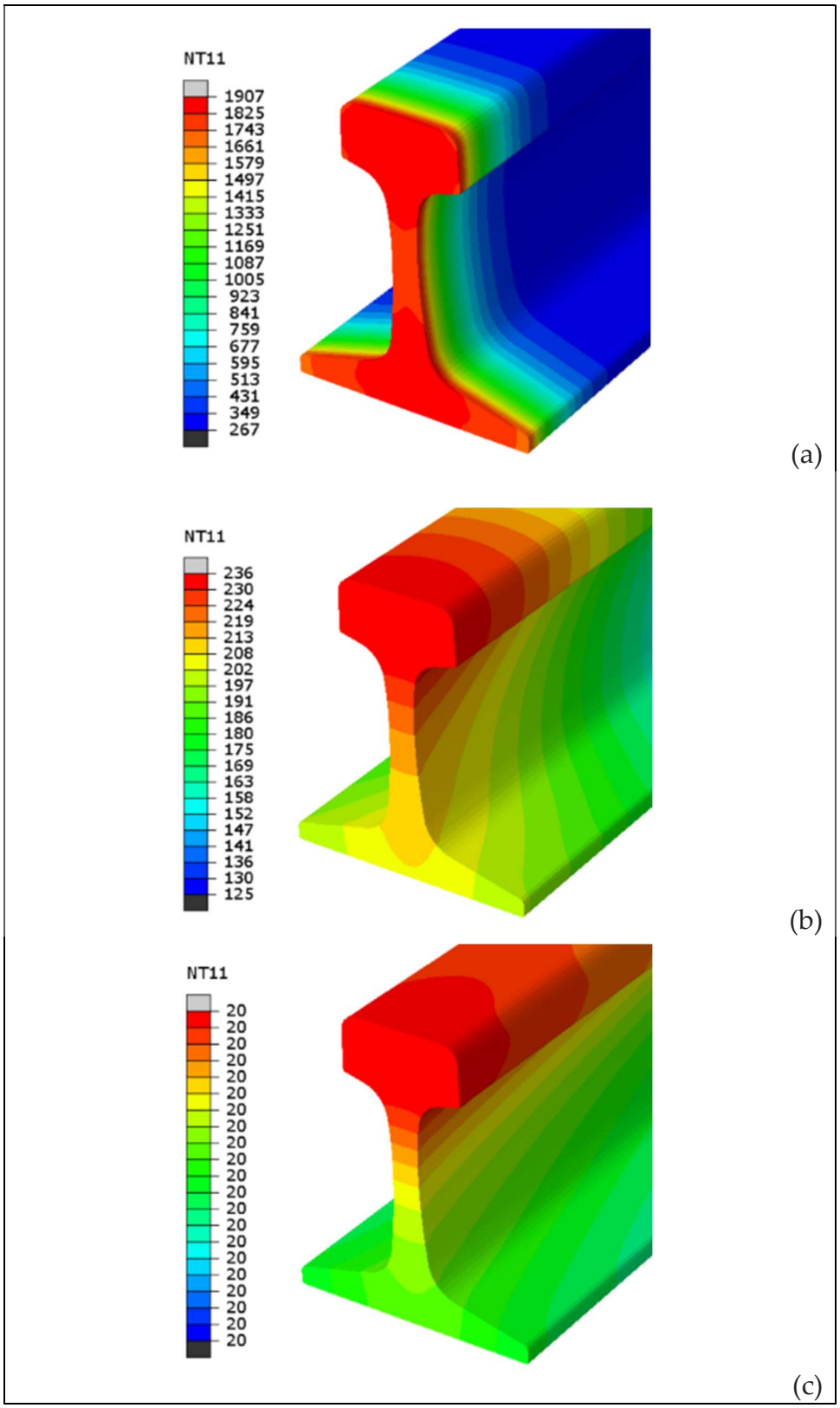

Figure 4.3: Weld fusion line temperature field evolution during welding (˚C) at (a) 70 sec, (b) 1 000 sec, and (c) 10 000 sec

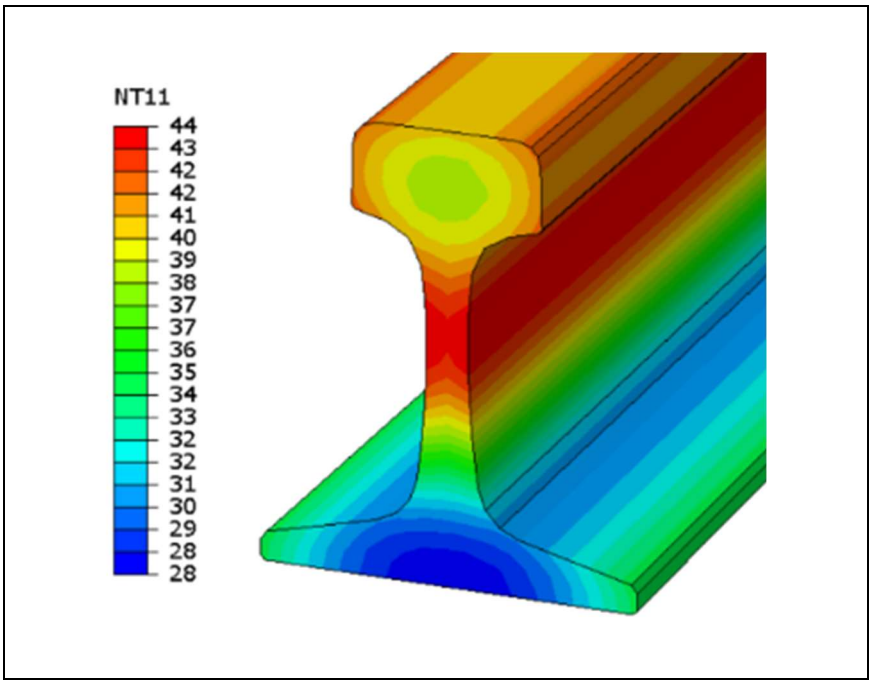

Figure 4.4: Peak rail temperature (˚C) during solar radiation cycle

4.4 Transverse Stress in Weldment

The transverse welding residual stress (Figure 4.5a) is characterized by a concentrated area of high tension at the center of the rail foot (385 MPa) and another concentrated area with medium-high tension at the core of the rail head (290 MPa). The web contains very nearly zero transverse stress. The combined stress (Figure 4.5c) in the weldment has similar distribution, although with different magnitudes. The comparison is displayed in Figure 4.6.

The transverse thermal stress (Figure 4.5b) is negligible throughout the entire rail. The noticeably high compression induced by the fasteners is completely isolated to the footprint of the idealized clip.

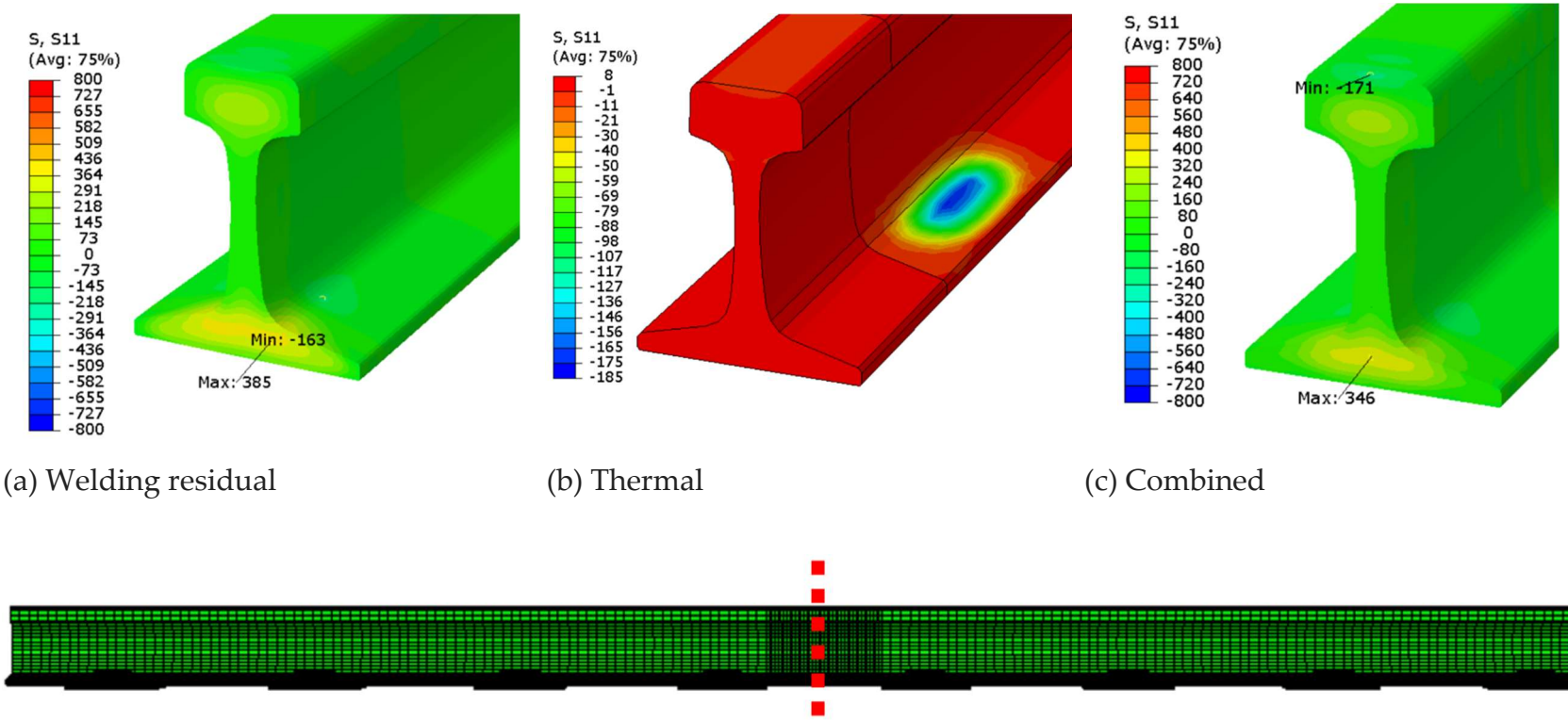

(a) Welding residual (b) Thermal (c) Combined

(d) Cross-sectional cut for transverse stress visualizations (above) and path in Figure 4.6

Figure 4.5: Transverse stress visualizations (MPa) at (d) weld cross-section for (a) welding residual, (b) thermal, and (c) combined

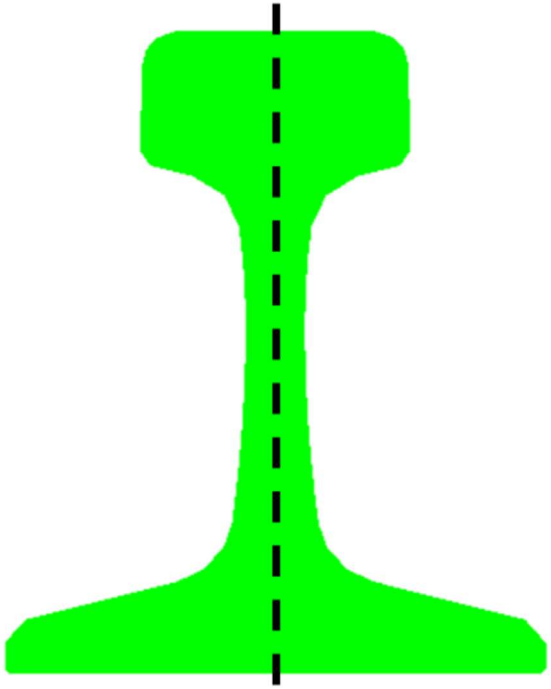

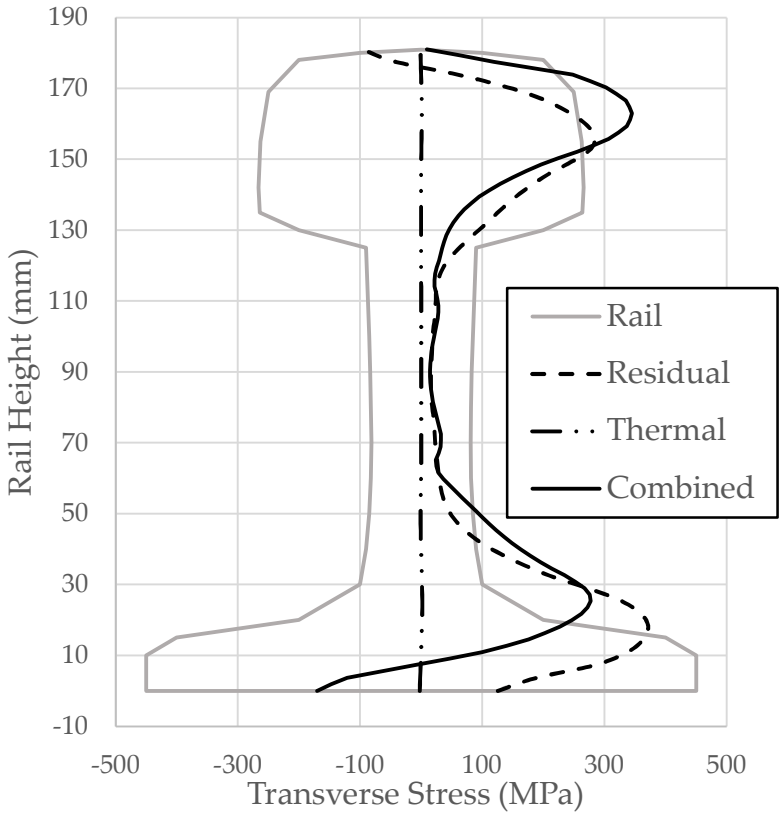

Vertical centerline path for chart to the right. Cross-sectional cut shown in Figure 4.5

Figure 4.6: Transverse stresses along weld vertical centerline path

4.5 Vertical Stress in Weldment

As seen in Figure 4.7, both welding residual and combined vertical stress distributions consist of high stress in the web (30-120 mm of rail height), which gradually dissipates through the rail head and foot.

The comparison of the welding residual and combined stresses along the vertical centerline path is shown in Figure 4.8, and the critical points of this comparison are tabulated in Table 4.1. Based on these results, the critical segments are the web and web to foot transition region, as displayed in Table 4.2. The discussion in Section 5.2 will focus on these two regions.

Table 4.1: Critical points for vertical stress

	Vertical Stress					
	y (mm)	**TH (MPa)**	**WR (MPa)**	**CB (MPa)**	**WR → CB**	**% Change**
Head	181	0.11	10.70	-125.78	-136.47	-1276%
	170	0.37	101.98	102.25	+0.27	+0%
	160	0.91	251.02	266.26	+15.24	+6%
	150	1.09	352.12	403.28	+51.16	+15%
	***140**	1.07	402.17	454.97	+52.80	+13%
Web	***120**	-0.08	548.40	490.50	-57.90	-11%
	110	-0.23	591.72	487.22	-104.49	-18%
	72	-0.32	571.52	497.87	-73.65	-13%
	60	-0.18	534.04	477.62	-56.41	-11%
	42	0.92	482.08	398.10	-83.97	-17%
	***30**	1.02	375.41	311.55	-63.86	-17%
Foot	***18**	0.60	223.92	185.54	-38.38	-17%
	***10**	0.30	121.11	75.98	-45.13	-37%
	3.5	0.13	31.88	10.88	-21.00	-66%
	0	0.03	13.85	3.72	-10.13	-73%

**Transition regions*

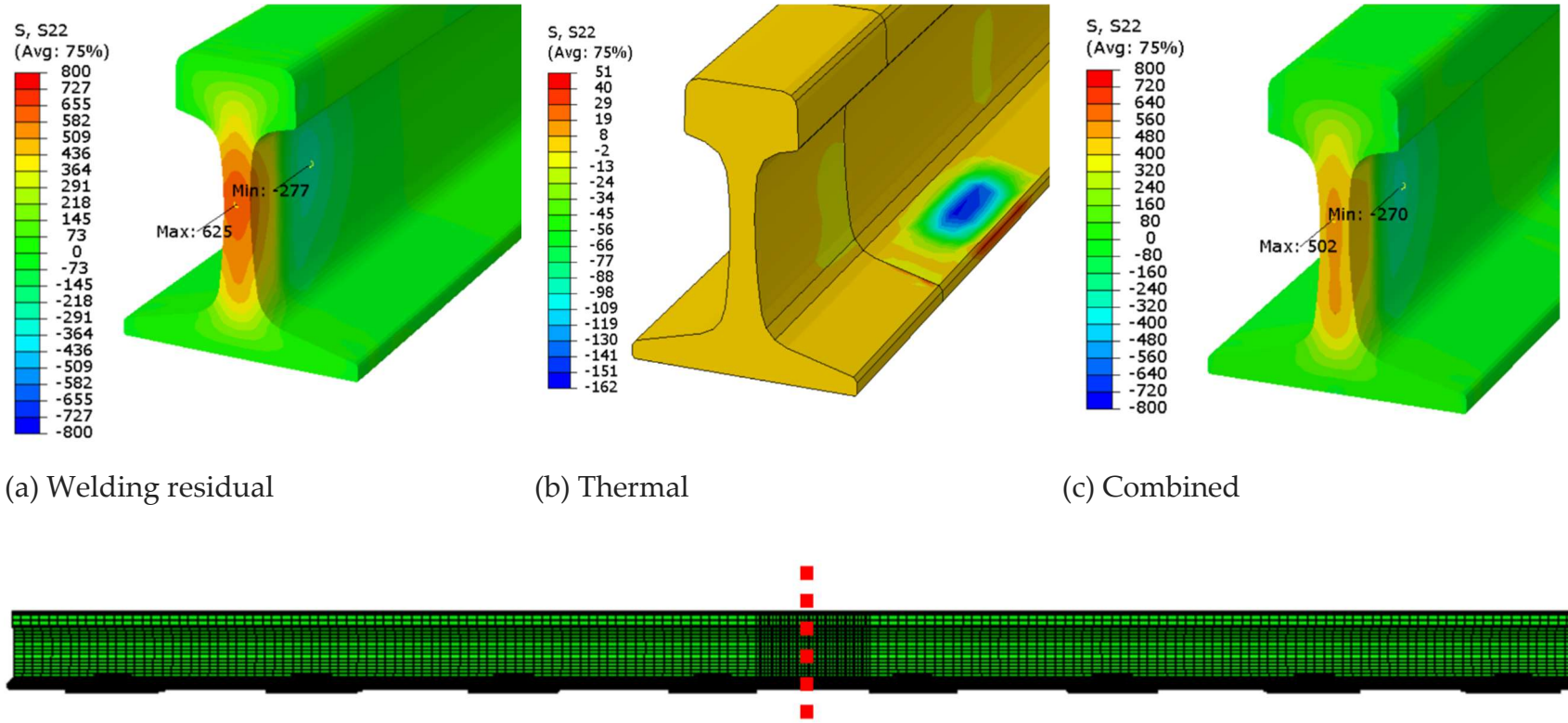

(a) Welding residual (b) Thermal (c) Combined

(d) Cross-sectional cut for vertical stress visualizations (above) and path in Figure 4.8

Figure 4.7: Vertical stress visualizations (MPa) at (d) weld cross-section for (a) welding residual, (b) thermal, and (c) combined

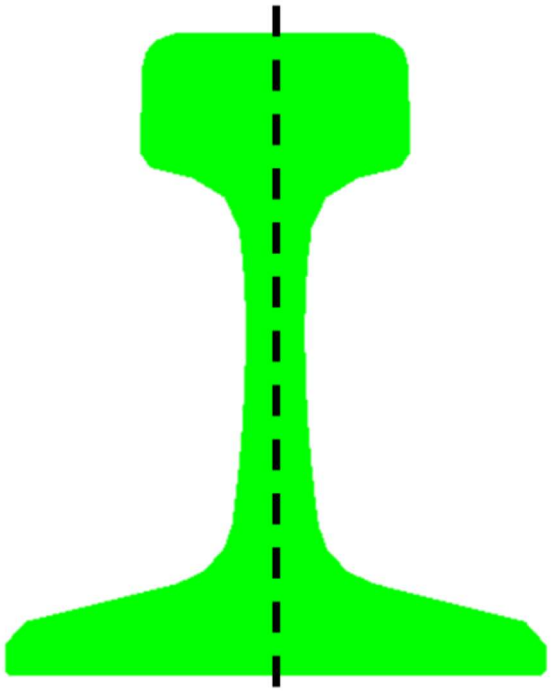

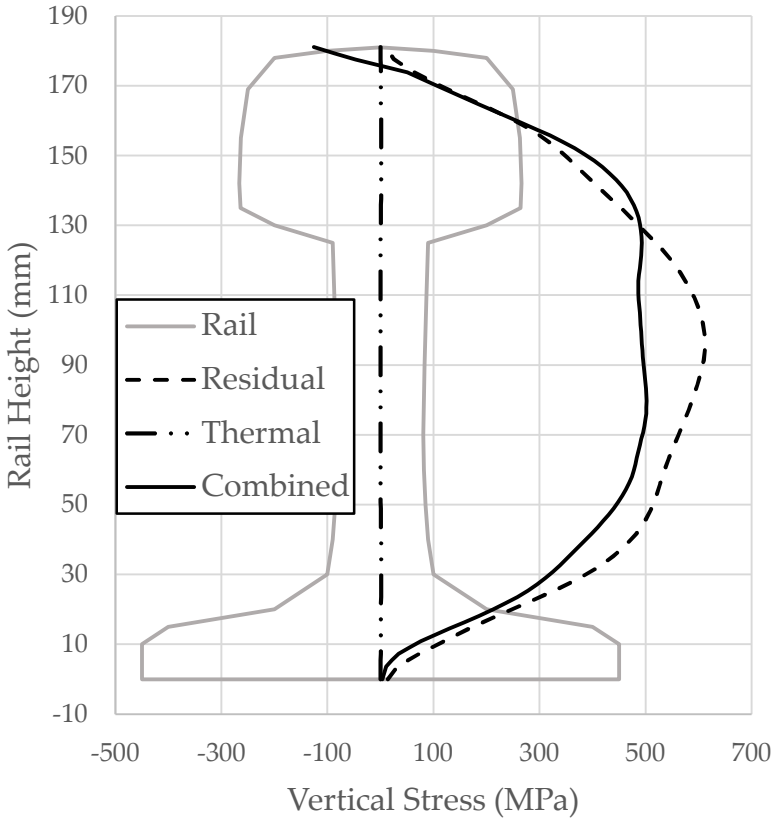

Vertical centerline path for chart to the right. Cross-sectional cut shown in Figure 4.7

Figure 4.8: Vertical stresses along weld vertical centerline path

Table 4.2: Critical segments for vertical stress

Segment	Average MPa Change (WR to CB)	Average % Change (WR to CB)
Web	-73.38	-14%
Foot to Web Transition Region	-49.12	-24%

The vertical thermal stress (Figure 4.7b) is negligible throughout the rail. The high compression spot seen is induced by the rail clip spring and is isolated to the footprint of the idealized clip.

4.6 Longitudinal Stress in Weldment

The longitudinal residual stress distribution (Figure 4.9a) is characterized by regions of concentrated tension in the cores of the rail head and foot, with a peak of 419 MPa. There is also compression along the edges of the rail head and foot, reaching values of -765 MPa. The combined stress (Figure 4.9c) shows a similar distribution, albeit relaxed.

The longitudinal thermal stresses are in compression, reaching -134 MPa in the rail foot, -147 MPa in the web, and -115 MPa in the rail foot. This disparity is mostly attributable to the section geometry, as disruptions from the fastener system appear to be localized.

A graphical comparison of the welding residual and combined stress is shown in Figure 4.10, with critical points presented in Table 4.3. This comparison

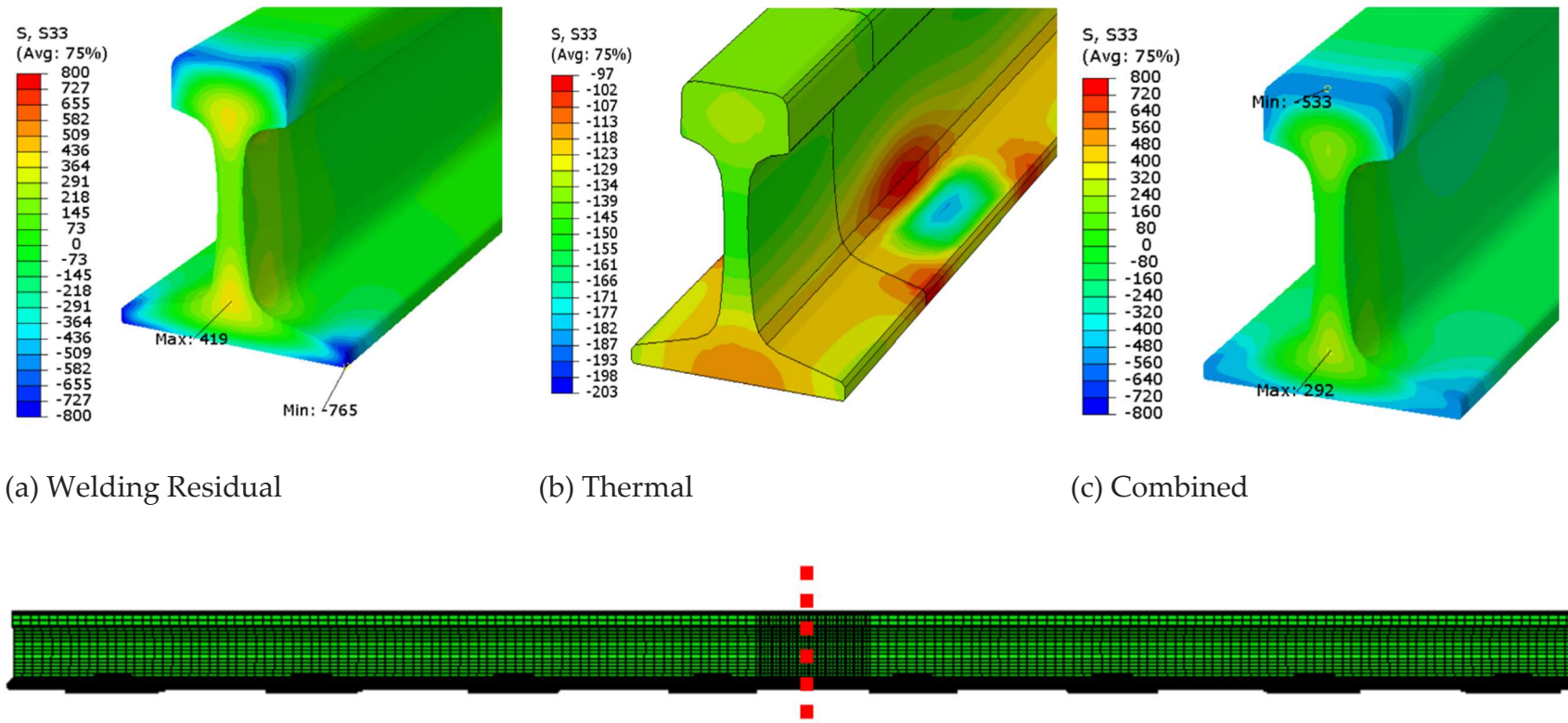

(a) Welding Residual (b) Thermal (c) Combined

(d) Cross-sectional cut for longitudinal stress visualizations (above) and path in Figure 4.10

Figure 4.9: Longitudinal stress visualizations (MPa) at (d) weld cross-section for (a) welding residual, (b) thermal, and (c) combined

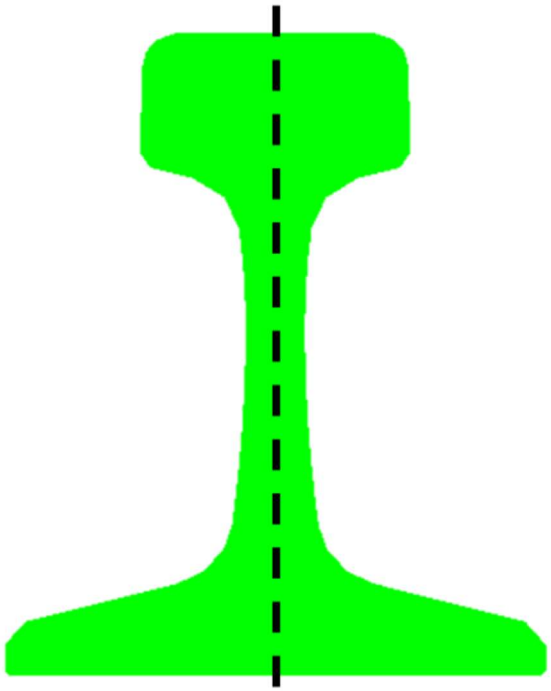

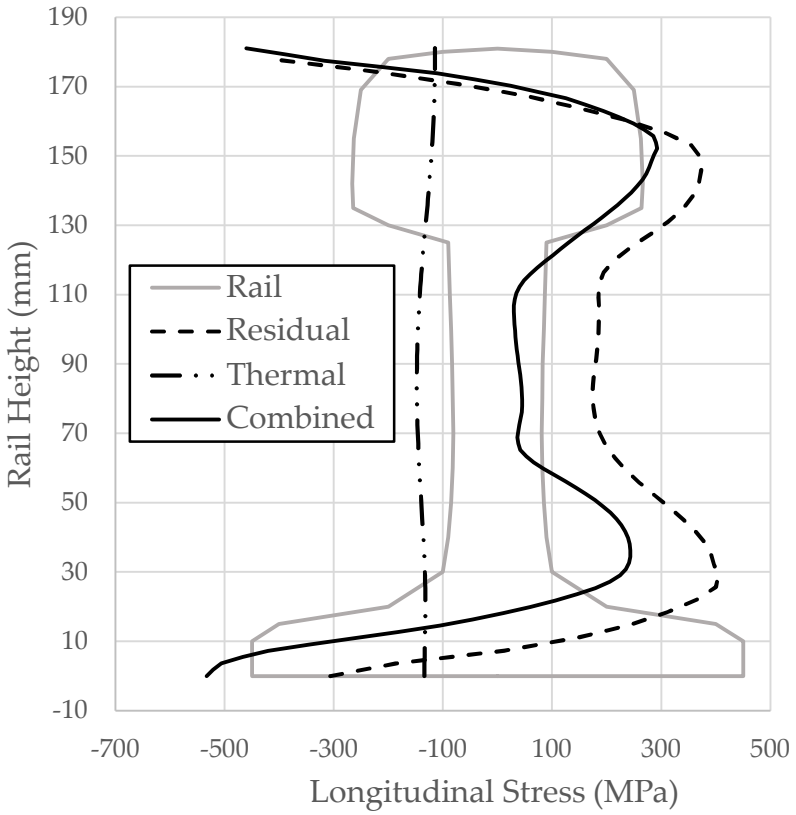

Vertical centerline path for chart to the right. Cross-sectional cut shown in Figure 4.9

Figure 4.10: Longitudinal stresses along weld vertical centerline path

is quite intricate, and all critical segments shown in Table 4.4 will be examined in Section 5.2.

Table 4.3: Critical points for longitudinal stress

	Longitudinal Stress					
	y (mm)	**TH (MPa)**	**WR (MPa)**	**CB (MPa)**	**CB → WR**	**% Change**
Head	181	-114.82	-500.10	-460.19	+39.91	+8%
	170	-115.32	-72.51	24.09	+96.60	+133%
	160	-117.85	238.98	249.28	+10.30	+4%
	150	-122.10	372.11	281.82	-90.28	-24%
	***140**	-125.78	368.87	255.61	-113.26	-31%
Web	***120**	-138.02	213.34	86.92	-126.42	-59%
	110	-143.04	184.59	31.76	-152.83	-83%
	72	-146.99	179.59	39.97	-139.62	-78%
	60	-143.38	235.56	84.78	-150.78	-64%
	42	-137.02	362.96	234.15	-128.81	-35%
	***30**	-133.07	404.17	224.56	-179.61	-44%
Foot	***18**	-132.52	311.91	10.87	-301.04	-97%
	***10**	-133.10	147.08	-265.06	-412.14	-280%
	3.5	-133.93	-186.77	-505.94	-319.17	-171%
	0	-134.35	-306.47	-533.26	-226.79	-74%

**Transition regions*

Table 4.4: Critical segments for longitudinal stress

Segment	**Average MPa Change (WR to CB)**	**Average % Change (WR to CB)**
Web to Head Transition Region	-119.84	-45%
Web	-146.34	-61%
Foot to Web Transition Region	-297.60	-140%
Foot	-319.37	-175%

4.7 Stress and Deformation 0.25m from Weld

The stress and deformation fields from the cross-sectional cut over a sleeper directly adjacent to the weld are shown in Figure 4.11. What is important to note is that these are the resultant fields from both *Model 2* and *Model 3*.

The physical system modelled was reduced in these simulations to the translational restrictions pertinent to the investigation of the weld. Therefore, the stress concentrations seen in Figure 4.11a, b, and c at the rail-clip and rail-plate interfaces should not be taken into consideration. Instead, these results are used to establish the extent of the weldment stress's influence, as discussed in Section 5.3.

4.8 Transverse Deformation in Weldment

The transverse thermal deformations are measured along a path that runs transversely along the foot, as this is where the largest expansion occurs. Due to the restraints and geometry of the rail, the centerline of the rail remains unmoved while the gauge and field edges of the rail head and foot expand. The maximum deformations are shown in Table 4.5 for further discussion in Section 5.3.

Table 4.5: Maximum transverse deformation in weldment

Causal Stress Type	**Maximum Deformation (μm)**
Welding Residual (WR)*	$\delta_{1,WR,max} = \emptyset$
Thermal (TH)	$\delta_{1,TH,max} = 58.8$
Combined (CB)	$\delta_{1,CB,max} = 43.5$

**Deformations from the welding process are assumed zero due to rail grinding.*

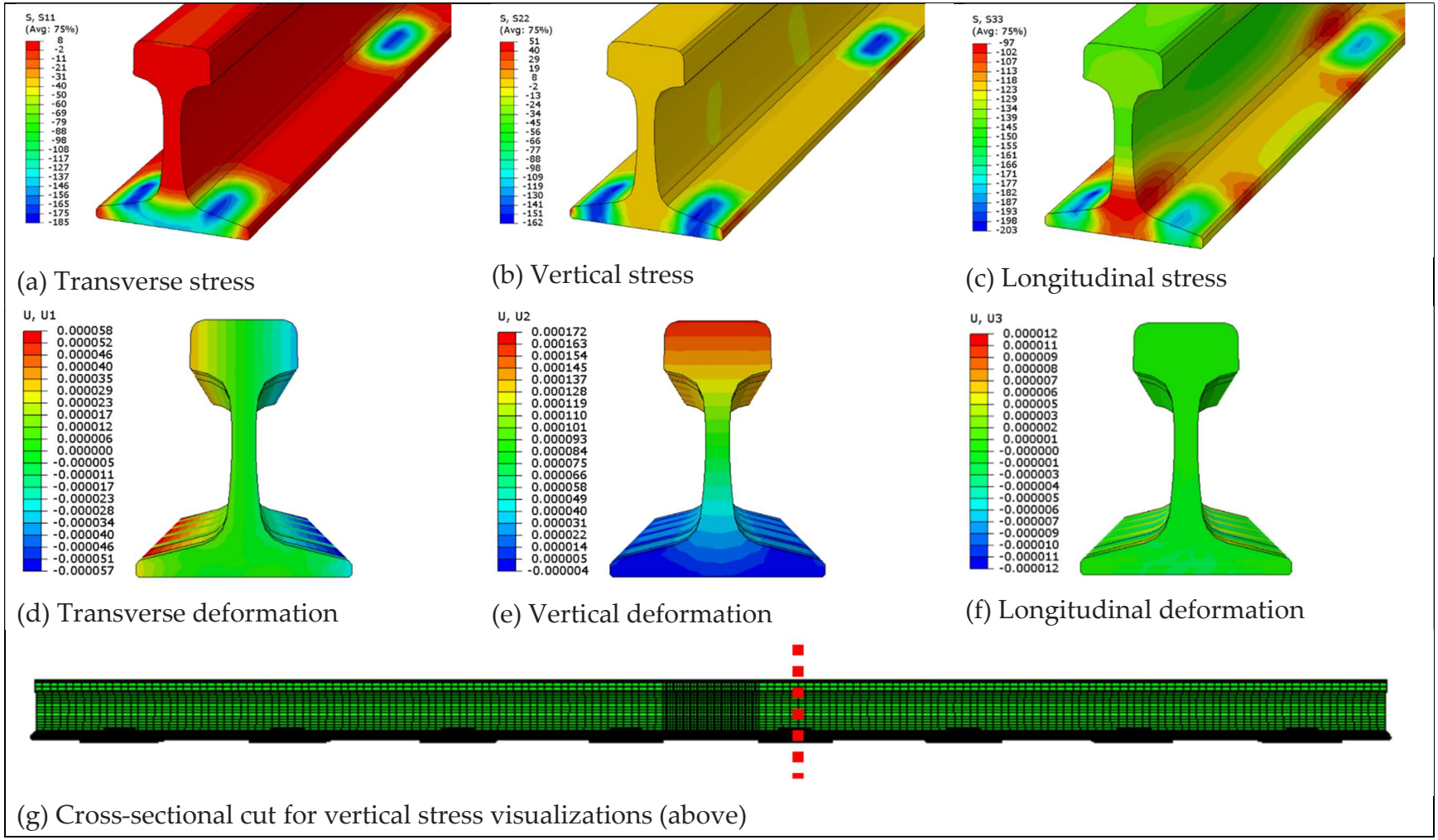

(a) Transverse stress

(b) Vertical stress

(c) Longitudinal stress

(d) Transverse deformation

(e) Vertical deformation

(f) Longitudinal deformation

(g) Cross-sectional cut for vertical stress visualizations (above)

Figure 4.11: Stress (MPa) and deformation (m) 0.25m from weld for both Model 2 and Model 3

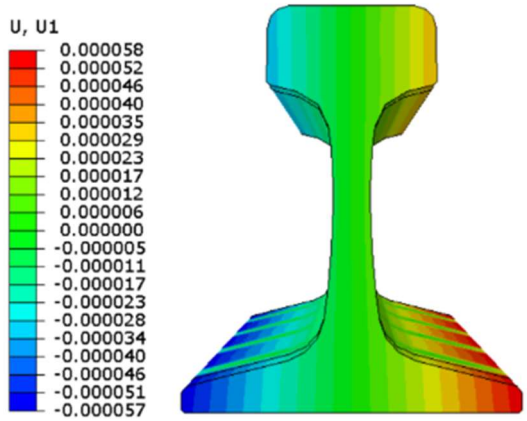

(a) Thermal

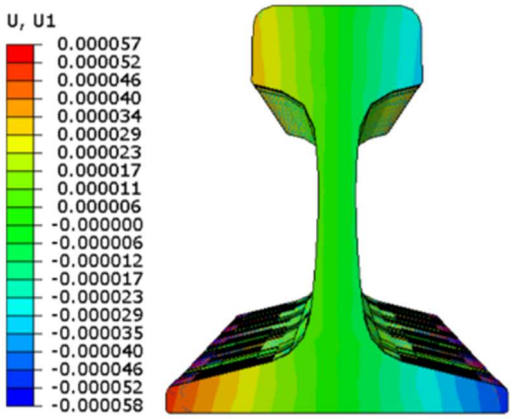

(b) Combined

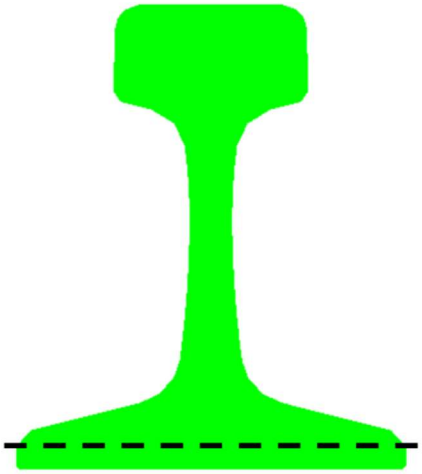

(c) Horizontal path for chart to the right. Cross-sectional cut shown in Figure 4.9

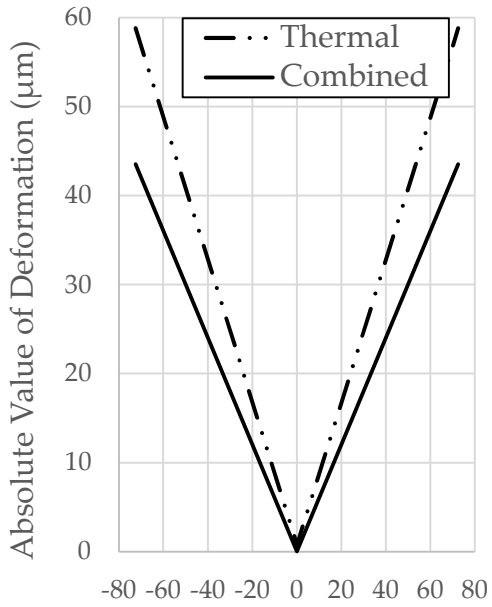

Figure 4.12: Transverse deformations (m) along (c) weld cross-section path for (a) thermal and (b) combined

4.9 Vertical Deformation in Weldment

The vertical expansion of the rail midspan of sleepers (Figure 4.13) is negligible at the base of rail height, where the restraining effects of the fastener system are felt. The expansion gradually increases with rail height before reaching the maximum at the top of rail running surface, which are shown in Table 4.6.

Table 4.6: Maximum vertical deformation in weldment

Causal Stress Type	**Maximum Deformation (μm)**
Welding Residual (WR)*	$\delta_{2,WR,max} = \emptyset$
Thermal (TH)	$\delta_{2,TH,max} = 170.9$
Combined (CB)	$\delta_{2,CB,max} = 163.4$

**Deformations from the welding process are assumed zero due to rail grinding.*

4.10 Vertical Deformation Along Top of Rail

Thermal expansion causes the rail to develop a longitudinal wave pattern along the top surface (Figure 4.14) that is highly dependent on sleeper/fastener spacing and material properties.

When a weld is not present (Figure 4.14b), the peak of this wave pattern occurs directly midspan of two sleepers and their corresponding fastener systems. This peak value is 171.5 microns in the presented configuration. The valley of the wave occurs directly atop the sleepers and reaches only 163.5 microns in the presented configuration.

When a weld is present (Figure 4.14c), and placed midspan of sleepers, there is a significant and abrupt distortion of the wave pattern. The peak that

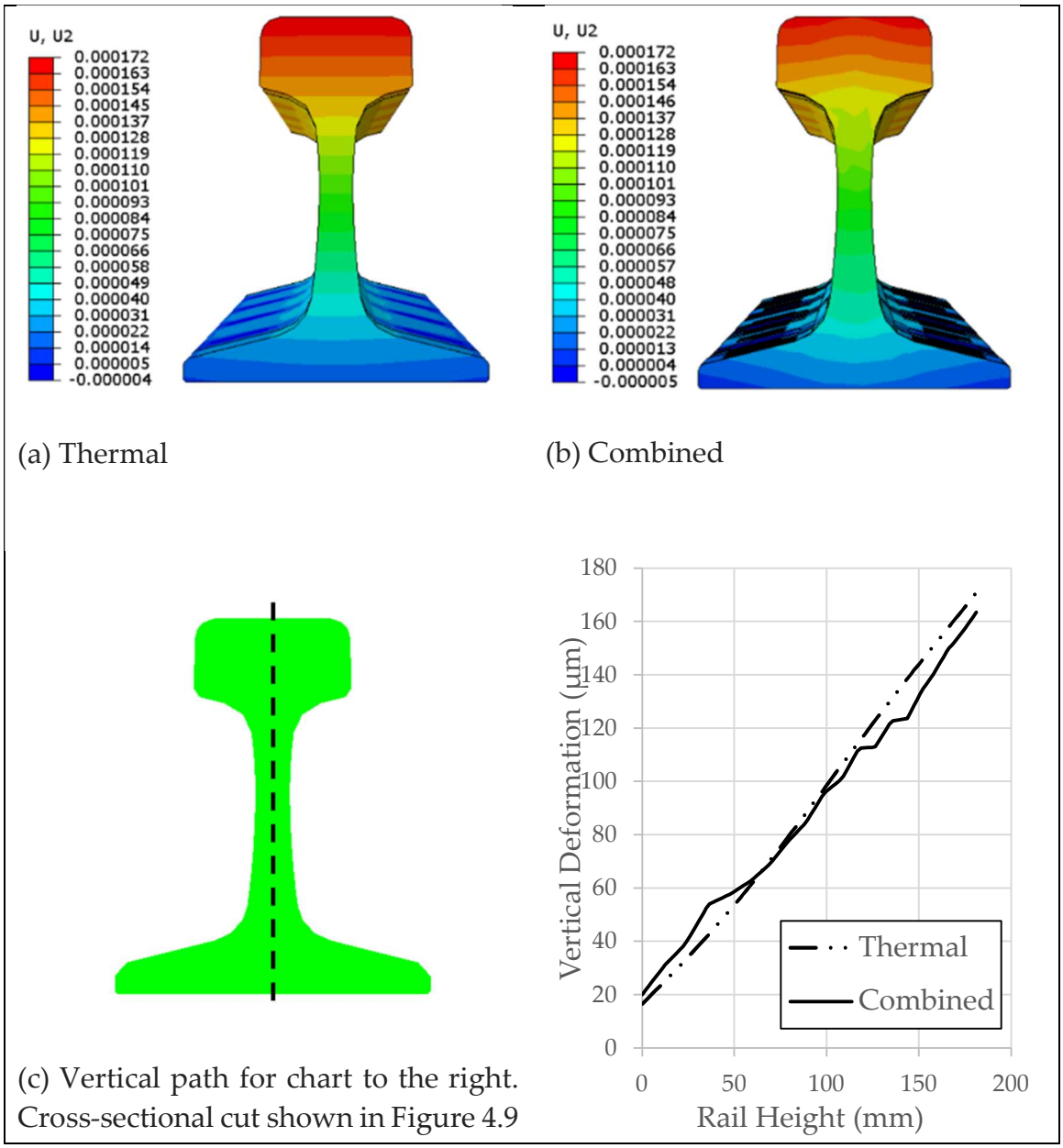

Figure 4.13: Vertical deformations (m) along (c) weld cross-section path for (a) thermal and (b) combined

would normally occur midspan instead presents as a valley of 163 microns. The detail and extent of the disruption is shown in the comparison of top surface deformation (Figure 4.14a). Additionally, the severity of this discontinuity can be quantified using the slope of the top surface deformation. Between 0 and 0.1 m

from the weld fusion line, the top surface slope with a weld is -2.57 times the slope without a weld.

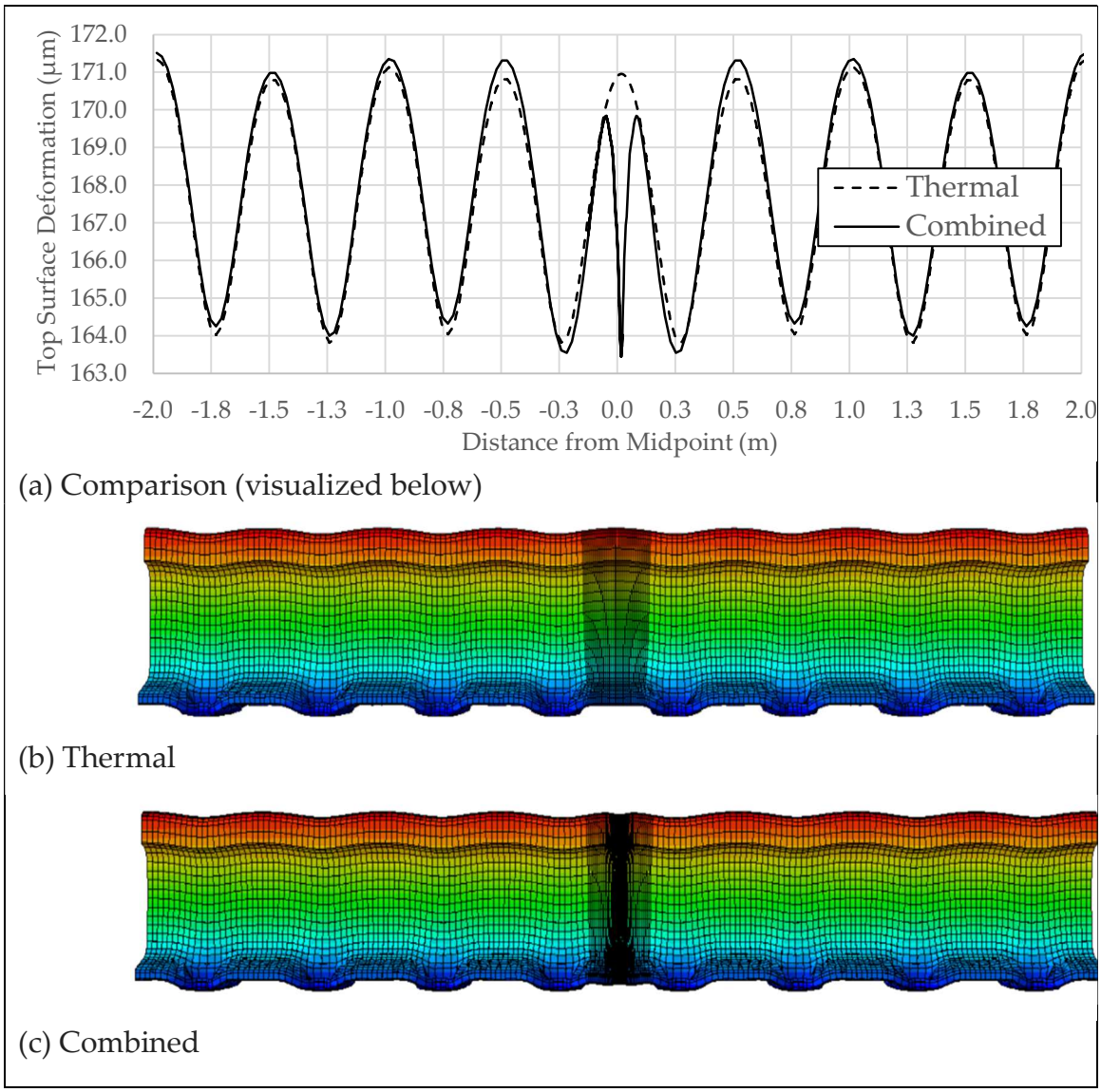

Figure 4.14: Top surface vertical deformation (a) comparison between (b) thermal and (c) combined

4.11 Longitudinal Deformation in Weldment

As seen in Figure 4.15 and Table 4.7, there is no longitudinal deformation throughout the rail, including the weldment, due to the continuous nature of the rail.

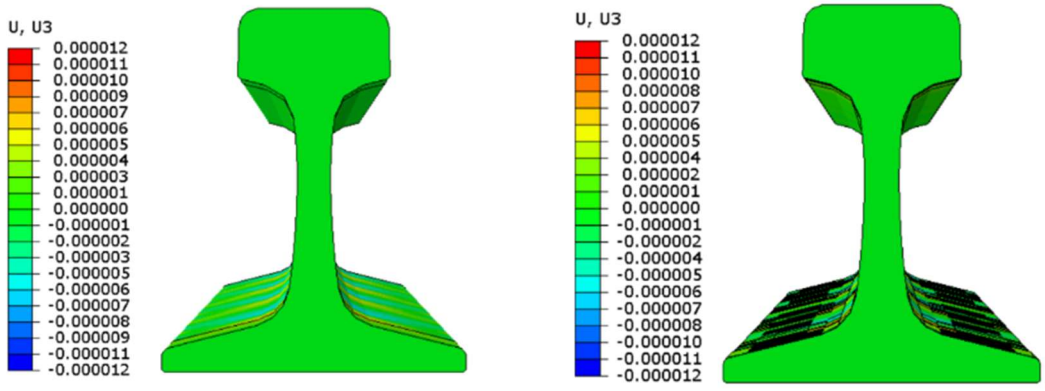

(a) Thermal (b) Combined

Figure 4.15: Longitudinal deformations (m) at weld cross-section for (a) thermal and (b) combined

Table 4.7: Maximum longitudinal deformations in weldment

Causal Stress Type	**Maximum Deformation (μm)**
Welding Residual (WR)*	$\delta_{3,WR,max} = \emptyset$
Thermal (TH)	$\delta_{3,TH,max} = 0.0$
Combined (CB)	$\delta_{3,CB,max} = 0.0$

**Deformations from the welding process are assumed zero due to rail grinding.*

Chapter 5 - Discussion

This chapter discusses the results presented in Chapter 4. The stress and deformation fields are considered in a manner similar to the results.

5.1 Temperature Fields

The temperature field evolution during the welding process, as depicted in Figure 4.3, helps explain the formation of residual stresses. The more exposed regions, such as the rail foot and web, would contract naturally due to the decrease in temperature were it not for the resistance offered by the hotter interior regions. The regions that cool first result in residual compression, while the regions that cool later result in residual tension.

When subjected to thermal loading, the rail heats to between 28 and 44 ˚C as seen in Figure 4.4. This temperature range is small enough that the thermal stress developed is relatively uniform (~20 MPa range) throughout the cross-section, especially when compared to the much larger range of welding residual stress (~800 MPa range).

The welding residual stress and stress developed by thermal expansion are uniquely linked by their thermal origins and will be examined in depth in the following section.

5.2 Stress Fields

The examination of stresses will focus on quantifying thermal expansion's impact on the welding residual stress.

In this study, when the rail temperature deviates 60 ˚C from RNT the total weldment stress changes significantly, as seen in Figure 4.6, Figure 4.8, and Figure 4.10. This change is nonuniform and the maximum tensile and compressive stress locations do not coincide between the welding residual stress (*Model 1*) and the combined weldment stress (*Model 3*). Therefore, measuring the amount of stress relaxation off peak values is inappropriate for this study. Instead, the following sections will examine the differences between the welding residual and combined stresses when averaged across the critical segments, as delineated in Table 4.2 and Table 4.4. Care is taken to average stress values of the same sign to avoid zeroing out the values. Quantifying the difference this way allows the risk associated with each critical region to be identified.

5.2.1 Transverse Stress Discussion

Results in Section 4.4

The transverse stress is not considered critical to rail operation, which mostly involves vertical and longitudinal stresses imparted to the rail. Therefore, this investigation focuses on the vertical and longitudinal distributions, and will not analyze the transverse stress in depth.

5.2.2 Vertical Stress Discussion

Results in Section 4.5

Across the web segment, the vertical stress in the weldment drops by an average of 73.4 MPa, or 14%, when subject to thermal expansion. The transition region between the foot and the web also drops in stress, although the magnitude of relaxation is smaller than that of the web itself. Since the vertical thermal stress is negligible throughout the entire cross section, the stress reduction cannot be attributed to combination of the welding and thermal stress. This reduction can, however, be attributed to the allowance of vertical deformation, as well as heating affects as discussed in-depth by Tawfik [8].

The vertical stress in the web remains in high tension, even when reduced by the thermal expansion. This daily tensile-to-tensile stress cycle places the web at risk of fatigue failures.

5.2.3 Longitudinal Stress Discussion

Results in Section 4.6

The relative uniformity of longitudinal thermal stress does not correlate to a uniform change from the welding residual to the combined stress distribution in the longitudinal direction. The foot and web drop by 320 MPa and 146 MPa respectively, while the head actually retains the entirety of the welding residual stress. This variance can be attributed to the following:

1) Combination of welding residual and thermal stress

- **a)** The stresses superimpose with small variance due to geometry of the cross-section.

2) Beam bending due to thermal deformation

- **a)** The bending of the rail between sleepers places the top fibers in tension and the bottom fibers in compression (Figure 5.1). This contributes tension that offsets some of the thermal compressive stress in the rail head. This also contributes more compression to the compressive stress in the foot.

3) Heating affects

- **a)** As before, heating affects as discussed by Tawfik account for some stress change [8].

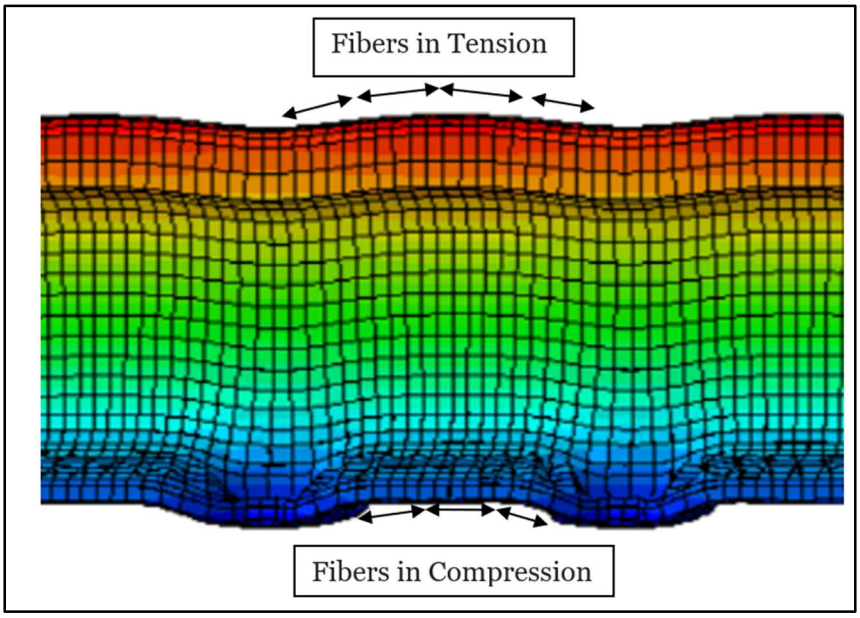

Figure 5.1: Beam bending of rail between sleepers

The uniform compressive thermal stress field developed in the rail impacts the weldment and the non-welded rail very differently. The non-welded rail has negligible initial longitudinal stress. When acted upon by daily solar radiation, a trivial-to-compressive stress cycle is induced. Additionally, the low magnitude of the thermal compressive stress corresponds to a lower risk of buckling in this portion of rail compared to the weldment.

In the weldment, two different stress cycles are created when the initial welding residual stress field undergoes thermal expansion. In the web and transition regions, initial tensile welding residual stresses are of higher magnitude than the compressive thermal stress. This generates a tensile-to-tensile stress cycle in these segments that risks fatigue failures. In the rail foot, the initial welding residual stresses are compressive. The thermal expansion results in a higher

compressive stress in this region, creating a compression-to-compression stress cycle. The high compressive stresses risk localized buckling or initiating global buckling.

5.3 Deformation Fields

The examination of deformations will focus on quantifying welding residual stress' impact on thermal expansion.

The maximum thermal deformations occur at the same locations when thermal expansion is modelled with a weld, *Model 3*, and without, *Model 2*. Therefore, the maximum deformation values will be utilized to quantify the impact of welding residual stress on thermal expansion and are shown in Table 4.5, Table 4.6, Table 4.7.

The welding residual stresses disrupt typical thermal expansion that occurs when the rail temperature deviates from the RNT by 60 ˚C. In the following sections, the level of disruption will be examined for each coordinate axis.

5.3.1 Transverse Deformation Discussion

Results in Section 4.8

The weld restricts 26% of transverse expansion, with a $\delta_{1,TH,max}$ of 58.8 microns and a $\delta_{1,CB,max}$ of 43.5 microns. While this is a significant level of restraint, the corresponding disruption to transverse deformation does not pose a serious risk to rail operation.

5.3.2 Vertical Deformation Discussion

Results in Section 4.9

The weld imposes a 4.4% (7.5 microns) restriction on vertical expansion at the weld fusion line, with a $\delta_{2,TH,max}$ of 170.9 microns and a $\delta_{2,CB,max}$ of 163.4 microns.

The slope of the graph in Figure 4.13 shows the rate of increase in vertical expansion as rail height increases. The thermal slope is steeper than the combined slope between 50 and 100 mm of rail height. This indicates the 4.4% of total restraint mostly occurs in this region, which corresponds to the web. This stands to reason, as the weldment web contains high vertical tensile stress that opposes vertical expansion.

The maximum expansion restraint by the weld occurs directly at the weld fusion line. As seen in the comparison of Figure 4.14a, this disruption to vertical deformation is mostly isolated to 150 mm from the weld fusion line. Disruption is, at most, 0.5 microns beyond 150 mm and fully dissipates past 800 mm from the weld fusion line. This is corroborated by the results from Figure 4.11, which shows that the stress and deformation fields are identical between *Model 2* and *Model 3*, indicating the effects of the weldment do not extend past the adjacent sleepers.

5.3.3 Longitudinal Deformation Discussion

Results in Section 4.11

The lack of longitudinal expansion seen in Figure 4.15 is expected and induces the longitudinal stress fields seen in Figure 4.9.

Chapter 6 - Conclusions

The presented investigation has clarified the combined effect of welding residual stress and thermal expansion. While the quantified results are specific to the presented rail configuration, the conclusions drawn are generally applicable.

6.1 Stress Fields

This investigation aimed to determine how thermal expansion impacted the weldment stress. This was intended to begin a discussion about including the combined stress field in rail design and fatigue life considerations, which are typically determined by bending stress imparted by vehicle loading. Through the process of this work, it is determined that the initial welding residual stresses are high enough to impact bending stress, possibly exceeding local strength of the steel. It is also discovered that the weldment undergoes a significant stress cycle when the rail thermally expands, possibly locally exceeding the fatigue endurance limit. How these localized affects should be considered in primary design is outside the scope of this thesis but is the next logical step for this work.

1) When railway is subjected to solar radiation, the stress field in the weldment changes. This causes a daily stress cycle in the weld that differs from the rail

at large. The initial welding residual stress field is heavily influenced by thermal stress, beam bending, and heating affects caused by thermal expansion.

a) The rail head has notably small changes longitudinally, retaining much of the welding residual stress.

b) In the web to head transition region, longitudinal stress decreases by 119.8 MPa (45%).

c) The web experiences drops of 73.4 MPa (14%) and 146.3 MPa (61%) in the vertical and longitudinal stresses, respectively.

d) The foot to web transition region sees drops of 49.1 MPa (24%) and 297 MPa (140%) in vertical and longitudinal stresses, respectively.

e) The rail foot drops by 319.4 MPa (175%) in longitudinal stress.

2) This daily stress cycle places the weldment at increased risk and helps explain the most frequent locations and types of rail failure.

a) The rail head does not have a stress cycle but does have high values of compressive longitudinal stress that contribute to risks of buckling or deformation of the running surface.

b) The web is characterized by tensile-to-tensile cycles in both vertical and longitudinal directions. The elevated values of stress throughout

the cycle risk fatigue failures, commonly manifesting as horizontal cracks.

c) The rail foot presents a compressive-to-compressive cycle longitudinally with high magnitudes of stress. This could contribute to global buckling or disrupt RNT estimations.

3) Stress turbulence from the weldment is localized.

a) The weldment fully dissipates 200 mm from the weld fusion line.

b) Within the weldment, the stress is governed by welding residual stress.

c) Beyond 200 mm from the weld fusion line, the stress is governed by thermal stress or vehicle load stresses when present.

6.2 Deformation Fields

This work sought to determine what impact initial stress has on thermal deformation. Vertical deformation is most pertinent to railway operation due to the restraints imposed by the fastener/sleeper system. By correlating the vertical stress with this vertical deformation, it was found that high tensile stress in the weld restrains vertical deformation, causing a discontinuity of the top surface. Since welded joints are susceptible to RSSI and other common rail failures due to local microstructural, stress field, and geometric discontinuities, this finding supports the concept that there are initial irregularities at the weld that grow to

larger problems when subjected to the high cycles of wheel loads during normal rail operation. The daily deformation cycle, as quantified here, should be helpful in future analysis, although ascertaining the level of risk this presents to train operation is outside the scope of this thesis

4) The vertical tensile stress in the weld web restricts vertical thermal expansion by 7.5 microns (4.4%) in the presented configuration.

- **a)** This determination is critical to Rizos's innovative method to measure RNT through top surface deformation [29]. This method, which looks promising for future use, should avoid measuring within 800 mm of a weld to ensure accurate results.
- **b)** Other non-destructive RNT measurement methods should also be examined in relation to the weldment. The chaotic nature of the weld, both in stress and deformation fields, could easily cause inaccurate measurements.
- **c)** The percent of restriction is exceedingly sensitive to changes in magnitude of vertical tensile stress in the weldment web.

5) The weldment stress field causes a severe disruption to the top surface.

- **a)** In non-welded rail, the top of rail surface wave pattern caused by restrained thermal expansion peaks between sleepers. When a weld is present, the typical peak reverses to a valley with a sharper gradient.

The behavior caused by this top surface distortion is reminiscent of the discontinuity present in bolted joints, which is the source of higher failure rates. However, the magnitude of this discontinuity is small and likely does not pose a risk to rail operation.

6) The impact of stress on deformation is isolated because of the localized nature of weldment stress.

a) The abrupt disruption to typical top surface vertical deformation occurs within 200 mm to either side of the weldment. There are negligible affects ($\leq$0.5 microns) up to 500 mm from the weld fusion line, which fully dissipate 800 mm from the weld.

b) The rail deformation atop a sleeper directly adjacent a weldment shows a negligible change (<0.1%) compared to a sleeper further away from the weldment.

6.3 Further Studies

Better understanding of welded joint behavior under combination loadings will allow consideration of innovative joint/rail design or modification that will improve railway safety and reduce costly failures. This paper can be the basis for future analyses including:

7) How should the stress concentrations and cycles be considered in rail design or fatigue endurance limit calculations?

a) The daily deviation from RNT varies based on season and region, corresponding to varied stress distributions. Perhaps a regionally dependent factor of safety could be added to allowable bending stress or fatigue endurance limit calculations.

b) The combined effects of welding residual stress, thermal expansion, and vehicle loading should be examined thoroughly to establish what this consideration should be.

8) Does the deformation discontinuity across the weld contribute to irregular vibrations in the wheel-rail system?

a) Could this impact the formation or propagation of RSSI?

9) Should the total weldment stress be considered in RNT calculations?

10) How do the results change when the rail configuration changes?

a) Includes rail temperature change, ambient temperature, sleeper spacing, fastener type, track modulus, rail shape, track curvature, and non-uniform heating of the rail.

11) What kind of change is needed at the weldment to reduce the deformation disruption and high stress concentrations?

a) Welding filler material, low solar absorption coatings, physical bracing, or possibly FRP.

References

[1] A. Skyttebol, B. L. Josefson and J. W. Ringsberg, "Fatigue Crack Growth in a Welded Rail Under the Influence of Residual Stresses," *Engineering Fracture Mechanics,* pp. 271-285, 2005.

[2] E. Johnson, "Measurement of Forces and Neutral Temperatures in Railway Rails - An Introductory Study," *Building Technology and Mechanics,* pp. 1-70, 2004.

[3] Federal Railroad Administration, Office of Safety Analysis, "Train Accidents by Railroad Group," [Online]. Available: https://safetydata.fra.dot.gov/officeofsafety/publicsite/Query/inctally3.aspx.

[4] P. J. Withers, "Residual Stress and Its Role in Failure," *Reports on Progress in Physics,* pp. 2211-2264, 2007.

[5] A. De and T. DebRoy, "A Perspective on Residual Stresses in Welding," *Science and Technology of Welding and Joining,* pp. 204-208, 2011.

[6] Y. Qian, *University of South Carolina, ECIV 580.*

[7] D. Tawfik, P. J. Mutton and W. K. Chiu, "Transient Thermal Stress Analysis on Rapid Post-Weld Heat Treatments Applied to Flash Butt Welded Rails," *Science and Technology in Welding and Joining,* pp. 326-336, 2013.

[8] D. Tawfik, P. J. Mutton and W. K. Chiu, "Modifying Residual Stress Levels in Rail Flash-Butt Welds Using Localized Rapid Post-Weld Heat Treatment and Accelerated Cooling," *International Heat Treatment and Surface Engineering,* pp. 126-130, 2008.

[9] D. Tawfik, P. J. Mutton and W. K. Chiu, "Experimental and Numerical Investigations: Alleviating Tensile Residual Stresses in Flash-Butt Welds by Localized Rapid Post-Weld Heat Treatment," *Journal of Materials Processing Technology,* pp. 279-291, 2006.

[10] D. Tawfik, O. Kirstein, P. J. Mutton and W. K. Chiu, "Verification of Residual Stresses in Flash-Buttt-Weld Rails Using Neutron Diffraction," *Physica B,* pp. 894-896, 2006.

[11] N. Ma, Z. Cai, H. Huang, D. Deng, H. Murakawa and J. Pan, "Investigation of Welding Residual Stress in Flash-Butt Joint of U71Mn Rail Steel by Numerical Simulation and Experiment," *Materials and Design,* pp. 1296-1309, 2015.

[12] Z. Cai, N. Ma, M. Nawafune, Y. Qu, B. Cao and H. Murakawa, "Residual Stresses in Flash Butt Welded Rail," *Transactions of JWRI,* pp. 79-87, 2011.

[13] L. Weingrill and N. Enzinger, "Temperature Field Evolution During Flash-Butt Welding of Railway Rails," *Materials Science Forum,* pp. 2088-2093, 2017.

[14] B. S. Oliveira, L. Rodrigues, E. Costa, E. Braga and M. Reis, "X-Ray Diffraction Analysis of Residual Stresses in the Premium Rails Welded by Flash Butt Process," *Soldagem and Inspecao,* pp. 1-9, 2019.

[15] S. H. Lee, S. H. Kim, Y. S. Chang and H. K. Jun, "Fatigue Life Assessment of Railway Rail Subjected to Welding Residual and Contact Stresses," *Journal of Mechanical Science and Technology,* pp. 4483-4491, 2014.

[16] Y. Sarikavak, O. S. Turkbas and C. Cogun, "Influence of Welding on Microstructure and Strength of Rail Steel," *Construction and Building Mateials,* pp. 1-8, 2020.

[17] M. Ghazanfari and P. H. Tehrani, "Investigation of Residual Stress and Optimization of Welding Process Parameters to Decrease Tensile Residual Stress in the Flash-Butt Welded UIC60 Rail," *Mechanics Based Design of Structures and Machines,* pp. 1-15, 2020.

[18] M. Ghazanfari and P. H. Tehrani, "Experimental and Numerical Investigation of the Characteristics of Flash-Butt Joints Used in Continuously Welded Rails," *Journal of Rail and Rapid Transit,* pp. 65-79, 2020.

[19] Schlatter Industries AG, [Online]. Available: https://railway-news.com/wp-content/uploads/2018/09/Schlatter-Rail-Welding-Brochure-.pdf.

[20] H. Murakawa, M. Beres, C. M. Davies, S. Rashed, A. Vega, M. Tsunori, K. M. Nikbin and D. Dye, "Effect of Low Transformation Temperature Weld Filler Metal on Welding Residual Stress," *Science and Technology of Welding and Joining,* pp. 393-399, 2013.

[21] H. Xiao, D. Yan, G. Liu and H. Wang, "Analysis on Mechanical Characteristics of Welded Joint With a New Reinforced Device in High-Speed Railway," *Advances in Mechanical Engineering,* pp. 1-15, 2020.

[22] Federal Railroad Administration, Office of Safety Assurance and Compliance, "Track Safety Standards Compliance Manual," United States Department of Transportation, Washington, D.C., 2008.

[23] Geography, [Online]. Available: https://geography.name/daily-and-annual-cycles-of-air-temperature/.

[24] Federal Railroad Administration, Office of Research and Development, "Track Buckling Prevention: Theory, Safety, Concepts, and Applications," United States Department of Transportation, Washington, D.C., 2013.

[25] J. Zakeri, S. Mohammadzadeh and M. Barati, "New Definition of Neutral Temperature in Continuously Welded Railway Track Curves," *Periodica Polytechnica, Civil Engineering,* pp. 143-147, 2018.

[26] Federal Railroad Administration, Office of Research, Development, and Technology, "Low Solar Absorption Coating for Reducing Rail Temperature and Preventing Buckling," United States Department of Transportation, Washington, D.C., 2018.

[27] J. Szelazek, "Monitoring of Thermal Stresses in Continuously Welded Rails With Ultrasonic Technique," *NDTnet,* pp. 1-8, 1998.

[28] T. Arts, "Measuring the Neutral Temperature in Railway Track During Installation and Use," *Graduate Report, Technical University Delft,* pp. 1-210, 2011.

[29] D.C. Rizos, "Non-Contact 3D-Vision System for Rail Neutral Temperature Measurements." International Application No: PCT/US2019/026267. 2018.

[30] K. Knopf, D. C. Rizos, Y. Qian and M. Sutton, "A Non-Contacting System for Rail Neutral Temperature and Stress Measurements: Concept Development," *Structural Health Monitoring,* pp. 84-100, 2020.

[31] Railway Tie Association, "Track/Traffic Density for US Class 1 and Short Line Railroads," 2008.

[32] L. Godefroid, G. L. de Faria, L. C. Candido and T. G. Viana, "Fatigue Failure of a Flash Butt Welded Rail," *Procedia Materials Science,* pp. 1896-1901, 2014.

[33] H. Farhangi and S. M. Mousavizadeh, "Horizontal Split-Web Fractures of Flash Butt Welded Rail," in *Proceedings of 8th International Fracture Conference*, Istanbul, Turkey, 2007.

[34] N. Ramadan, K. Tur and E. Konca, "Process Design Optimization for Welding of the Head Hardened R350 Ht Rails and Their Fatigue: A Literature Review," *International Journal of Engineering Research and Development,* pp. 2278-800, 2017.

[35] J. C. Nielson, R. Lundén, A. Johansson and T. Vernersson, "Train-Track Interaction and Mechanisms of Irregular Wear on Wheel and Rail Surfaces," *Vehicle System Dynamics*, 40 (1-3), 3-54, 2003.

[36] S. Kaewunruen, M. Ishida and S. Marich, "Dynamic Wheel-Rail Interaction Over Rail Squat Defects," *Acoustics Australia,* 43 (1), 97-107, 2015.

[37] J. Xu, P. Wang, Y. Gao, J. Chen and R. Chen, "Geometry Evolution of Rail Weld Irregularity and the Effect on Wheel-Rail Dynamic Interaction in Heavy Haul Railways," *Engineering Failure Analysis,* 81, 31-44, 2017.

[38] D. Uzarski, *Railroad Track Design Including Asphalt Trackbeds,* 2009.

[39] Dassault Systemes Simulia Corp., "Abaqus 6.11 Theory Manual," 2011.

[40] MatWeb, "AISI 1084 Steel, Hot Rolled Bar (UNS G10840)," [Online]. Available: http://www.matweb.com/search/datasheet_print.aspx?matguid=1702681fd5b2456e8e0c5932ba9b3f28.

[41] AREMA, "Manual for Railway Engineering," 2010.

[42] X. K. Zhu and Y. J. Chao, "Effects of Temperature-Dependent Material Properties on Welding Simulation," *Computers & Structures,* pp. 967-976, 2002.

[43] R. Masoudi, M. Shariati and K. Farhangdoost, "3D Finite Element Simulation of Residual Stresses in UIC60 Rails During The Quenching Process," *Thermal Science,* pp. 1301-1307, 2017.

[44] A. Kalup, B. Smetana, M. Kawulokova, S. Zla, H. Francova, P. Dostal, K. Waloszkova, L. Waloszkova and J. Dobrovska, "Liquidus and Solidus Temperatures and Latent Heats of Melting of Steels," *Journal of Thermal Analysis and Calorimetry,* pp. 127:123-128, 2017.

Appendix A - Additional Numerical Model Data

Additional welding residual stress distribution paths from *Model 1* are provided here for completeness. Model results are compared to experimental data points from Ma [11] and visualized distributions from Tawfik [10] and Oliveira [14].

A.1 Top Surface Path (See Figure A.1)

Considering that Ma averages the strain across 14 mm to determine the stress, the presented top surface path seems to be in good agreement with Ma's data. While Tawfik did not obtain results for this path, Oliveira's transverse distribution is of similar shape. The presented results are not in agreement with Oliveira's longitudinal distribution, which has small tensile forces in at the fusion line dropping into small compression outside the HAZ before returning to neutral. The presented vertical distribution is flat and therefore omitted from this graph.

A.2 Bottom Surface Path (See Figure A.1)

The results presented have obvious differences to the experimental data from Ma, but these can be accepted given the sharp gradients of the transverse and

longitudinal calculated predictions. Neither Tawfik nor Oliveira obtained results for this path. The presented vertical distribution is flat and therefore omitted from this graph.

A.3 Center of Rail Head Path (See Figure A.2)

Ma did not obtain results for this path. Longitudinal results from both Tawfik and Oliveira agree well with presented results. However, both have vertical distributions that slope down to neutral at a slower rate than the presented results. However, since those results are used to generally gauge the shape of the distribution, the presented results can be reasonably accepted.

A.4 Web Surface Path (See Figure A.2)

For this path, Ma only reported one data point (strain gauge averaged over 14 mm) for each coordinate direction, and it is difficult to establish agreement with the presented results. However, Tawfik's vertical distribution shapes agrees with the presented shape, starting at a slightly lower tensile force in the fusion line before dropping to compression and returning to neutral. Oliveira did not obtain results for this path. The presented transverse distribution is flat and therefore omitted from this graph.

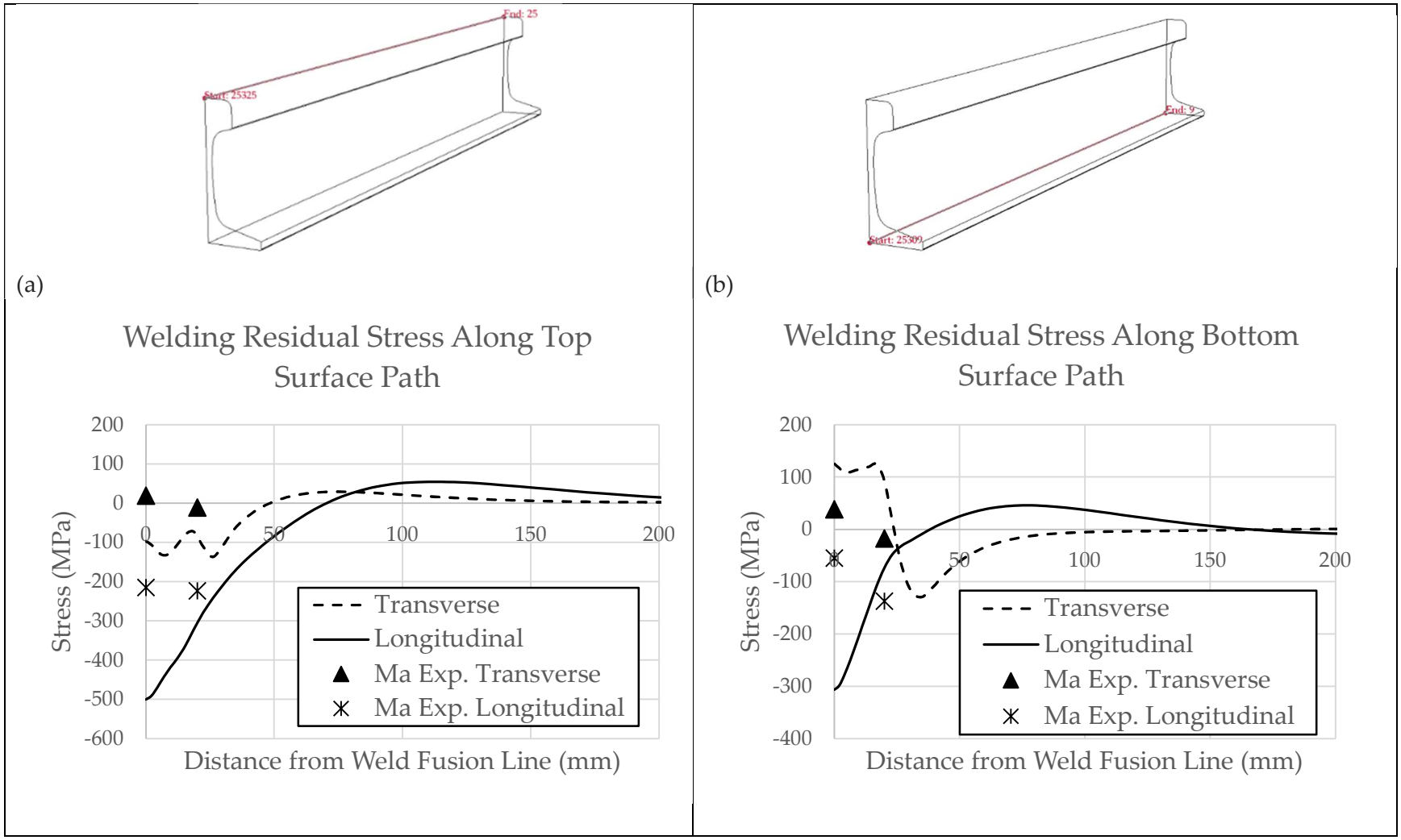

Figure A.1: Top (a) and bottom (b) surface paths for welding residual stress

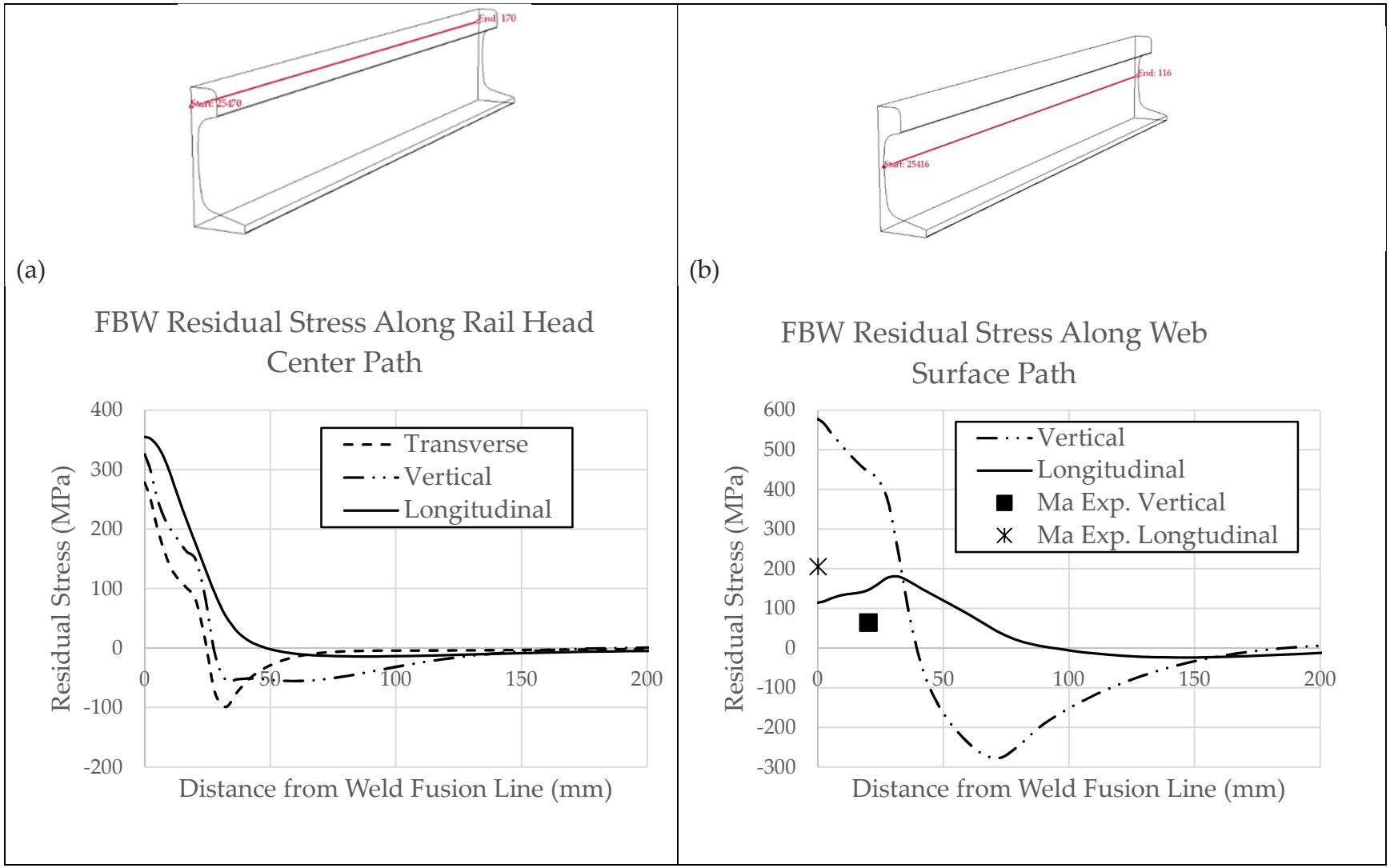

Figure A.2: Rail head center (a) and web surface (b) paths for welding residual stress

Appendix B - Abaqus Equations

The governing mechanical equilibrium equation is written in the classical form of virtual work, utilizing a Lagrangian approach as shown in Equation B.1. Output for this study was the standard Cauchy "true" stress tensor, as this is the direct measure of the traction being carried per unit area by any internal surface.

$$\int_V \sigma : \delta D \, dV = \int_S \delta v \cdot t \, dS + \int_V \delta v \cdot f \, dV \qquad \textit{Equation B.1}$$

where V is the volume occupied, S is the surface bounding the volume, t is the surface traction at any point on S (force per unit area), f is the body force at any point within V (force per unit volume), δv is the "virtual" velocity field, and δD is the rate of deformation. t, f, and σ are an equilibrium set:

Force equilibrium over the volume is: $\int_S t \, dS + \int_V f \, dV = 0$

Cauchy stress matrix at point of S is defined by: $t = n \cdot \sigma$

Stress matrix must be symmetric: $\sigma = \sigma^T$

Translational equilibrium is: $\left(\frac{\vartheta}{\vartheta x}\right) \cdot \sigma + f = 0$

The governing thermal energy balance equation (Green & Naghdi) is taken as:

$$\int_V \rho \dot{U} \, dV = \int_S q \, dS \int_V r \, dV \qquad \textit{Equation B.2}$$

where V is the volume of solid material, S is the surface area of the solid, $\dot{U}$ *is the material time rate of the internal energy,* ρ *is the material density, and r is the heat supplied externally to the body per unit volume.*

The thermal constitutive equation accounts for specific heat affects, while latent heat effects from phase changes are considered in the material properties:

$$c(\theta) = \frac{dU}{d\theta} \qquad \textit{Equation B.3}$$

where c is specific heat, θ is temperature, and U is displacement.

Heat conduction is modelled using Fourier's Law, and is isotropic for the presented material:

$$f = -k\frac{\delta\theta}{\delta x} \qquad \textit{Equation B.4}$$

where k is the conductivity matrix, f is the heat flux, and x is the position.

Heat loss due to convection is modelled using Newton's Law of Cooling:

$$q_c = -h_c(T_s - T_0) \qquad \textit{Equation B.5}$$

where is q_c heat loss to convection, h_c is the convection coefficient, T_s is the surface temperature, and T_0 is the ambient temperature.

Heat loss due to radiation is modelled using the Stefan-Boltzmann Law:

$$q_r = -\varepsilon\sigma\{(T_s - 273)^4 - (T_0 - 273)^4\} \qquad \textit{Equation B.6}$$

where q_r is the heat loss to radiation, ε is the emissivity factor, and σ is the Stefan-Boltzmann constant (5.67E-08 W/m²K)

Appendix C - Verification of Simplified Temperature Dependent Material Properties

The presented investigation used AISI 1084 steel (Table 3.1) with simplified temperature-dependent properties because the full temperature-dependent material properties were not available at the time of this writing. Shown here is the procedure used to verify the simplification of temperature-dependent material properties proposed by Zhu [33].

The procedure for *Model 1* outlined in Chapter 3 was run twice. One analysis was run using the temperature dependent material properties for UIC grade 900A steel (Table C.3) obtained by Skyttebol [1]. The other analysis used material properties simplified using Zhu's method (Table C.2). This allowed a comparison of the simplified values to the "true" values.

The peak welding residual stresses were extracted from the weld fusion line cross-section for both analyses and shown in Table C.1. The simplified values provide results with an average 6.6% change, assuming the full temperature-dependent properties provide the "true" results. This % change is in line with

Zhu's results and deemed acceptable, and the procedure was implemented with AISI 1084 steel.

Table C.1: Full and simplified UIC grade 900A model results

Direction	Stress Type	Full (MPa)	Simplified (MPa)	%Δ
Transverse	Tension	472.8	435.4	7.9
	Compression	-191.2	-178.5	6.6
Vertical	Tension	713.1	643.8	9.7
	Compression	-291.4	-301.9	3.6
Longitudinal	Tension	483.4	498.9	3.2
	Compression	-683.1	-742.1	8.6
				6.6%

Table C.2: UIC grade 900A simplified properties

Property	UIC grade 900A (Simplified)		
Temperature (˚C)	**20**	**100**	**>980**
Density (kg/m³)	7 800		
Emissivity	0.96		
Thermal Expansion Coefficient (m/m/˚C)	1.33E-05		
Convection Coefficient (W/[m²-˚C])	27		
Latent Heat of Fusion (J/kg)	296 000		
Poisson's Ratio	0.3		
Specific Heat Capacity (J/[kg-˚C])	460		
Temperature of Liquidus (˚C)	1 526		
Temperature of Solidus (˚C)	1 470		
Thermal Conductivity (W/[m-˚C])	47.5		
Young's Modulus (MPa)	210 000		
Yield Stress (MPa)	430	430	21.5
Fracture Stress (MPa)	806	806	40.3

Table C.3: UIC grade 900A temperature-dependent properties

Temperature (˚C)	13	20	40	115	315	415	515	600	615	715	1040	1240	1470
Density (kg/m³)	7800												
Emissivity	0.96												
Thermal Expansion Coefficient (m/m/˚C)		13.3						15.7					17.4
Convection Coefficient (W/[m²-˚C])	27.0												
Latent Heat of Fusion (J/kg)	296 000												
Poisson's Ratio		0.3						0.3					0.4
Specific Heat Capacity (J/[kg-˚C])			460		589	632	669		679	669.1	685.8		
Temperature of Liquidus (˚C)	1526												
Temperature of Solidus (˚C)	1470												
Thermal Conductivity (W/[m-˚C])	47.57			48.07	41.85		35.64			29.21	26.86	29.53	
Young's Modulus (MPa)		210 000						110 000					10 000
Yield Stress (MPa)		430						242					20
Fracture Stress (MPa)		806						350					25

*Values are linearly interpolated between points

Appendix D - Metric/English Conversion Factors

Table D.1: Unit conversion factors

Units of Length			Units of Area		
1 micrometer (μm)	≈	3.9E-05 inch (in)	1 square millimeter (mm^2)	≈	1.6E-03 square inch (in^2)
1 millimeter (mm)	≈	0.04 inch (in)	1 square centimeter (cm^2)	≈	0.16 square inch (in^2)
1 centimeter (cm)	≈	0.4 inch (in)	1 square meter (m^2)	≈	10.8 square feet (ft^2)
1 meter (m)	≈	3.3 feet (ft)			1.2 square yards (yd^2)
		1.1 yards (yd)	1 square kilometer (km^2)	≈	0.4 square mile (mi^2)
1 kilometer (km)	≈	0.6 mile (mi)			247.1 acres
					100 hectares (ha)
Units of Volume			**Units of Weight-Mass**		
1 milliliter (ml)	≈	0.03 fluid ounce (fl oz)	1 gram (gm)	≈	0.036 ounce (oz)
1 liter (l)	≈	4.22 cups (c)	1 kilogram (kg)	≈	2.2 pounds (lb)
		0.26 gallon (gal)			0.068 slug
1 cubic millimeter (mm^3)	≈	6.1E-05 cubic inch (in^3)	1 tonne (t)	≈	1.1 short tons
1 cubic meter (m^3)	≈	36 cubic feet (ft^3)			1 000 kilograms (kg)
		1.3 cubic yards (yd^3)	**Units of Force**		
			1 newton (J/m)	≈	0.22 pound-force (lbf)
Units of Pressure			**Units of Temperature**		
1 pascal (Pa)	≈	1.4E-04 pound per square inch (psi)	°F → °C		$C = {}^{5}/_{9}\,(F - 32)$
1 megapascal (MPa)	≈	0.14 kilopound force per square inch (ksi)	°C → °F		$F = {}^{9}/_{5}\,C + 32$

Table D.2: Metric prefixes

giga (G-)	mega (M-)	kilo (k-)	hecto (h-)	deca (da-)	unit (-)	deci (d-)	centi (c-)	milli (m-)	micro (μ-)	nano (n-)
10^9	10^6	10^3	10^2	10^1	1	10^{-1}	10^{-2}	10^{-3}	10^{-6}	10^{-9}

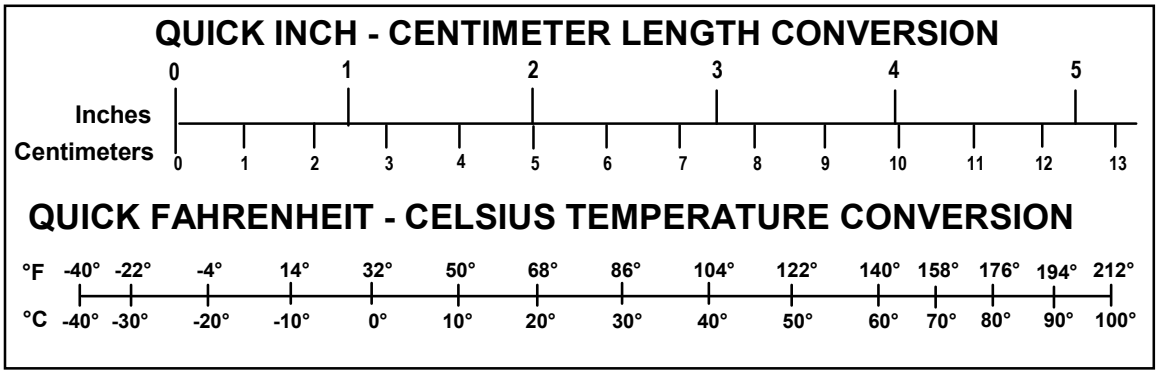

Figure D.1: Quick conversions for inch-centimeter and Fahrenheit-Celsius